# Coupling Suspended Sediment Dynamics and Light Penetration in the Upper Chesapeake Bay

May 23, 2006

Charles L. Gallegos, E. Amy Lewis, and Hae-Cheol Kim

Smithsonian Environmental Research Center
P. O. Box 28
Edgewater, MD 21037

## Table of Contents

## List of Figures

## List of Tables

**List of Notation**

| Symbol | Definition |
|---|---|
| | Water Quality Parameters |
| CDOM | Colored dissolved organic matter |
| CHLA | Phytoplankton chlorophyll-*a* |
| TSS | Total suspended solids |
| | Inherent Optical Properties (IOPs) |
| $a_t$ | Total absorption coefficient |
| $a_w$ | Absorption coefficient of water |
| $a_{t\text{-}w}$ | Total absorption coefficient less that due to water |
| $a_g$ | Absorption coefficient of CDOM |
| $a_p$ | Absorption coefficient of particulate matter |
| $a_\phi$ | Absorption coefficient of phytoplankton |
| $a_{p\text{-}\phi}$ | Absorption coefficient of non-algal particulates (NAP) |
| $b_p$ | Particulate scattering coefficient |
| $b_b$ | Scattering that is directed upward |
| $B=b_b/b$ | Backscattering fraction |
| $c=a_t+b_p$ | Beam attenuation coefficient |
| $a_\phi^*(675)$ | Specific-absorption coefficient of phytoplankton chlorophyll at 675 nm |
| $a_{p\text{-}\phi}^*(440)$ | Specific-absorption coefficient of TSS at 440 nm |
| $b_p^*(555)$ | Specific-scattering coefficient of TSS at 555 nm |
| $\lambda$ | Wavelength of light |
| | Spectral Shape Parameters |
| $g(\lambda)=a_g(\lambda)/a_g(440)$ | Normalized absorption spectrum of CDOM |
| $\phi(\lambda)=a_\phi(\lambda)/a_\phi(675)$ | Normalized absorption spectrum of phytoplankton chlorophyll |
| $p(\lambda)=a_{p\text{-}\phi}(\lambda)/a_{p\text{-}\phi}(440)$ | Normalized absorption spectrum of non-algal particulates |
| $b_n(\lambda)=b_p(\lambda)/b_p(555)$ | Normalized scattering spectrum |
| $b_n^\phi(\lambda)$ | Normalized spectrum describing suppression of scattering in algal absorption bands |
| $s_g$ | Spectral slope of absorption by CDOM |
| $s_p$ | Spectral slope of absorption by NAP |
| $\eta$ | Spectral exponent of scattering of particulate scattering |
| $\phi_i$ | Scale parameter for suppression of scattering in algal absorption bands |
| | Geometric Parameters |
| Z | Depth in the water column |
| *sza* | Solar zenith angle |
| $\mu_0$ | Cosine of the *sza* after refraction at the air-water interface |
| $\Gamma=cZ$ | Optical depth |
| | Apparent Optical Properties |
| $E_d$ | Downwelling, cosine-corrected irradiance |
| $K_d$ | Diffuse attenuation coefficient |
| $\kappa_0$ | Empirical coefficient relating surface $K_d$ to IOPs |
| $\kappa_z$ | Coefficient relating $K_d$ at varying optical depths to IOPs |

## Background

The attenuation of light underwater is an important process in estuaries, directly affecting phytoplankton, submerged aquatic vegetation (SAV), visually orienting predators, and indirectly affecting oxygen depletion and other indicators of water quality. It is, therefore, important that ecosystem models simulating such processes have an accurate algorithm for simulating light attenuation from the concentrations of materials that absorb and scatter light.

Three water quality constituents contribute to light attenuation in estuaries: colored dissolved organic matter (CDOM) absorbs light selectively at blue wavelengths; phytoplankton chlorophyll *a* (CHLA) both scatters and absorbs light, having absorption peaks at blue and red wavelengths; and suspended solids (TSS) scatter and absorb light, with absorption predominately in the blue wavelength region. The problem of modeling light attenuation in estuaries, therefore, consists of specifying the contribution of water itself plus the three optically active water quality constituents to the absorption and scattering of light, then relating absorption and scattering to light attenuation using relationships derived from radiative transfer theory.

The absorption and scattering coefficients are inherent optical properties, which have the advantageous property that their values are proportional to the concentration of the causative factor. That is, we can model the absorption due to, e.g. chlorophyll, as

$$a_\phi(\lambda) = a_\phi^*(\lambda)[CHLA]$$

where λ=wavelength of light, $a_\phi(\lambda)$=absorption due to phytoplankton, and $a_\phi^*(\lambda)$=specific-absorption spectrum of phytoplankton chlorophyll. Similar expressions can be written for absorption by other constituents, as well as for scattering. In this work, specific-absorption and -scattering spectra were determined from field measurements and water samples collected on the Potomac River.

In a series of papers, Kirk (1981, 1984, 1994) established a relationship between the diffuse attenuation coefficient, $K_d$, an apparent optical property, and the inherent optical properties, total absorption coefficient, $a_t$, and particulate scattering coefficient, $b_p$, which took the form,

$$K_d(\lambda) = \frac{1}{\mu_0}\sqrt{a_t^{\,2}(\lambda) + G(\mu_0)a_t(\lambda)b_p(\lambda)} \qquad (1)$$

where $\mu_0$ is the cosine of the solar angle of incidence after refraction at the air-water interface, and $G(\mu_0)$ is a function of $\mu_0$ that scales the effect of scattering on attenuation. $G(\mu_0)$ was found to be a linear function of $\mu_0$, i.e. $G(\mu_0)=g_1\mu_0-g_2$, where the coefficients $g_1$ and $g_2$ depended on the optical depth of interest (Kirk 1984), and the shape of the scattering phase function (Kirk 1994). [The scattering phase function specifies the directional distribution of scattering. Most scattering in natural waters is strongly in the forward (i.e. downward) direction, with generally only a small fraction, <1 to ~4%, in the backward (upward) direction].

A number of the assumptions used by Kirk limit the applicability of equation 1 for use in shallow, turbid waters. For example, Kirk's Monte Carlo simulation of underwater light

propagation considered only the direct solar beam, whereas diffuse sky light is always present. Kirk (1994) formulated the effect of variations in the shape of the scattering phase function in terms of its average cosine; but the scattering phase function is not amenable to routine measurement, unlike the backscatter fraction, $B$ (i.e. the ratio of backscattering to total scattering $B=b_b:b$) for which commercial instrumentation is available. Most importantly, Kirk (1994) only gave formulae for calculating $g_1$ and $g_2$ for the 1% optical depth, i.e. the depth at which incident irradiance is reduced to 1 percent of its surface value. Seeing, however, that $a_t$ and $b_p$ in equation 1 are functions of wavelength, the 1% optical depth also will necessarily be a function of wavelength. Stated differently, at any depth of interest, each wavelength potentially will be at a different optical depth. This is especially problematic in applications in which simulation of growth of submerged aquatic vegetation (SAV) is of primary interest, as SAV generally require more light than phytoplankton (e.g. ca. 20-25% of surface light for mesohaline and polyhaline species, 9-13% for tidal fresh and oligohaline species, Batiuk et al. 2000).

Alternative expressions for calculating $K_d$ from $a_t$ and $b_p$ have been proposed, that may offer some improvement in computational efficiency over equation 1. Albert and Mobley (2003) used a simplified expression to relate $K_d$ to absorption and backscattering,

$$K_d = \kappa_0 \frac{a_t + b_b}{\mu_0} \tag{2}$$

and found that the coefficient, $\kappa_0$ had a value of 1.0546; but they did not vary $B$ in their simulations, and they calculated $K_d$ for small depth increments, rather than from the surface to the depth of interest, as is needed for this work. Here we performed radiative transfer simulations using the program *Hydrolight*™ to determine values for $\kappa_0$ as a function of $B$, $\mu_0$, $b:a$ ratio, and optical depth, $cZ=(a+b)Z$. Field data for initial application and evaluation of the model were collected from the Potomac River, primarily tidal fresh and oligohaline zones.

## Methods

### Radiative Transfer Modeling

*Hydrolight*™ is a commercially available program that provides an exact solution to the equations of radiative transfer in water. *Hydrolight* includes a model of diffuse sky irradiance as well as provision for specifying the shape of the scattering phase function in terms of the backscatter probability, $B$ (Mobley 1994). In this work we used *Hydrolight* to simulate the propagation of light underwater at a wide range of values for $a_t$, $b_p$, $\mu_0$, and $B$ in nested loops (Table 1). For each simulation we calculated $K_d$ from the surface down to a range of depths such that the percentage of light remaining was just $\geq$0.1% of immediately subsurface irradiance. At each depth we calculated the coefficient $\kappa_z$ by rearrangement of equation 2 (note change in symbol from $\kappa_0$ to $\kappa_z$, because it is now a function of optical depth). The simulation procedure resulted in 2,880 separate runs of *Hydrolight*, and 48,960 realizations of $K_d$ and $\kappa_z$. We reduced this number to 42,694 realizations by omitting large optical depths, where the downwelling irradiance was less than 0.01% of surface values, i.e. much less than the photic depth. We then determined simple algebraic expressions for $\kappa_z$, and hence also, $K_d$, in terms of the governing variables, optical depth $\Gamma=c\cdot z$, backscatter fraction $B$, scattering:absorption ratio $b/a$, and cosine

of the refracted solar incidence angle $\mu_0$, by successive application of empirical parametric curve fitting (see below).

Table 1. Range of parameter variation in simulations with *Hydrolight*, used to determine an empirical model for calculating $K_d$ from $a$, $b$, and backscattering.

| Parameter | Symbol | Minimum | Maximum | Increment | Number |
|---|---|---|---|---|---|
| Solar zenith angle | *sza* | 0 | 75 | 15 | 6 |
| Backscatter fraction, $b_b/b$ | $B$ | 0.006 | 0.042 | 0.004 | 10 |
| Scattering:absorption ratio | $b/a$ | 0.25<br>10<br>15 | 10<br>49 | Variable<br>5 | 40<br>8 |
| Optical depth, $c \cdot z$ | $\Gamma$ | 0 | 40 | Variable | 17 |

Field and Laboratory Methods.

*Axial Cruises.* The Potomac River was sampled quarterly from March 2004 to November 2005 (March, June, August/September, November). SERC personnel did not participate in the November 2004 cruise. Traveling upstream, thirteen stations were sampled from below the US-301 Bridge to above the Woodrow Wilson Bridge in both the Potomac and Anacostia Rivers (PR01-PR13, Figure 1). Of the latter two stations, one was in the Anacostia River (PR12) and one was in the Potomac River (PR13). Originally, eight of these stations coincided with those used by the Chesapeake Bay Monitoring Program. However, two of these stations (PR02, PR10) were moved slightly during the course of study in order to sample deeper sites in the river. Stations PR02a and PR03 occasionally required second casts without the AC9 or VSF due to cable length restrictions.

On station, an instrument package was deployed in the water just below the surface (Figure 2). The package consisted of a WETLabs absorption and attenuation meter (AC9) and backscattering meter (ECO VSF3) provided by SERC, as well as sensors for conductivity, temperature, depth, dissolved oxygen (YSI SBE23), scalar photosynthetically active radiation (PAR, Licor), particle-size (LISST-100), transmittance at 660 nm (10cm WETLabs Cstar transmissometer), optical backscattering turbidity (D&A OBS 3) and algal fluorescence (WETLabs WETStar), provided by UMCES HPL. Also, an ADCP provided by VIMS was mounted at the bow.

At the first station for each cruise, the AC9 depth sensor was calibrated. Surface water samples (0.5m) were collected by pumping through 19 mm inner diameter pvc tubing. The water intake was located centrally within the instrument package. The pump was turned on and allowed to flush for one minute before collecting water samples. After collecting surface water samples the package was lowered to approximately one meter above the bottom. If bottom samples were collected, the pump was allowed to flush for one minute prior to collection. Samples were immediately placed in coolers with ice. Two bottles were filled for each sample, 2 liters with no preservatives for optical water quality analyses and 250 mL fixed with formalin for bacterial cell counts. Water samples were taken from 0.5m depth at every station and from one meter above the bottom at seven stations (PR03, PR05, PR07, PR08, PR09, PR10 and PR13).

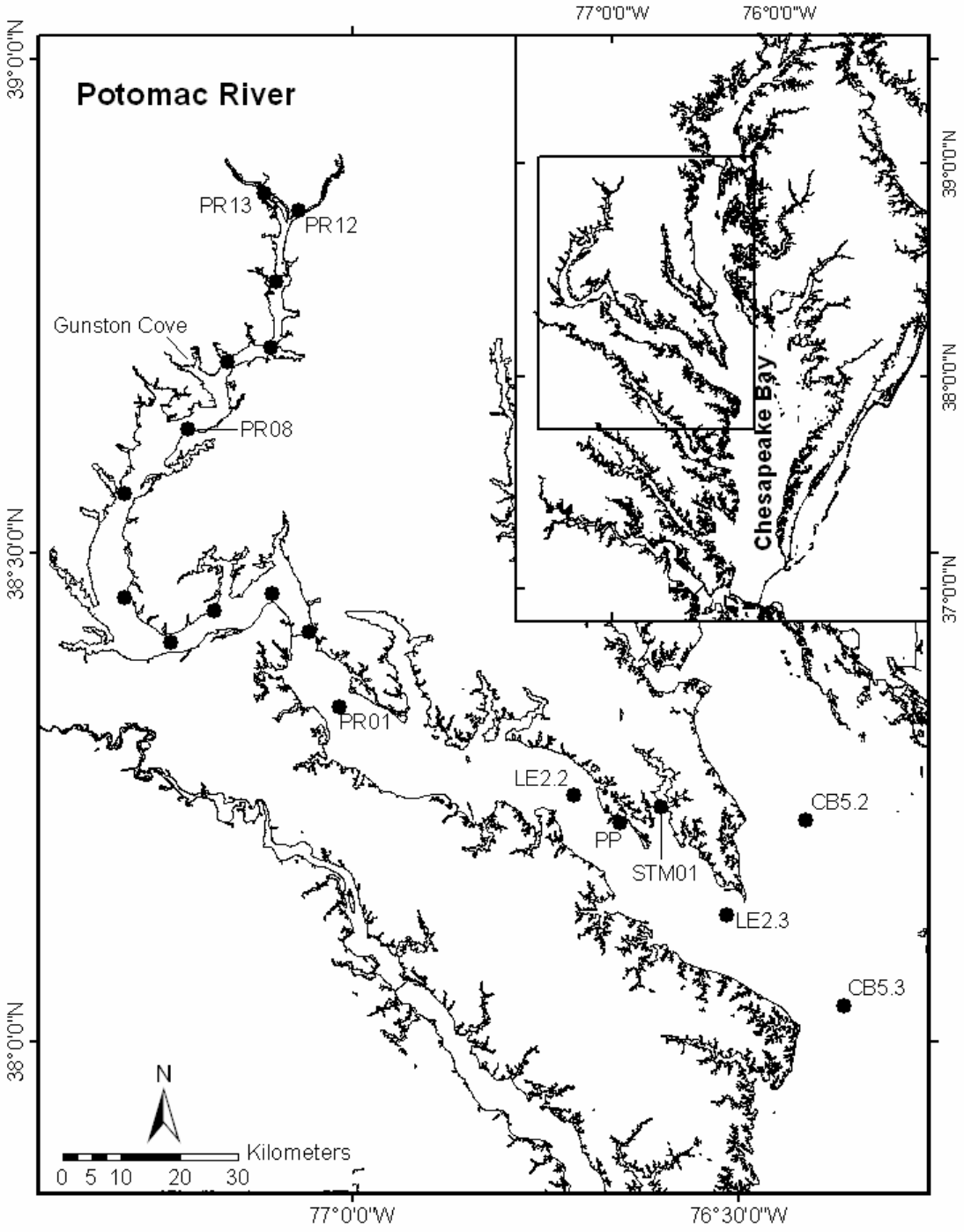


Figure 1. Map of field stations. Axial cruise stations are numbered incrementally from PR01, south of the US-301 bridge to PR13, in downtown Washington, D.C.; not all station names are shown. Station STM01 is located in the St. Marys River. The area of the 2004 tidal intensive survey is labeled Gunston Cove.

Water samples were transported back to the laboratory on ice, and kept refrigerated at 4ºC overnight. The next morning, the water samples were filtered for chlorophyll, particulate absorption and colored dissolved organic matter. In addition, samples were analyzed for absorption and scattering coefficients (by procedures of Gallegos and Neale 2002) and turbidity. Aliquots were sent to the SERC Analytical Services Laboratory for total suspended solids analysis.

*Tidal Intensive.* Part of the intensive tidal survey on August 26, 2004 involved a lateral survey at Gunston Cove, between stations PR08 and PR09. A SERC-owned Boston Whaler was used for our part of the lateral survey. Four stations were sampled repeatedly from approximately two hours before to three hours after slack water (low tide) in order to collect data at several different current velocities. Stations A-D were located in a lateral transect across the river with station A inside of Gunston Cove, station B in the channel and stations C and D on the opposite shoal. Station B was in proximity to the buoy and VIMS's *R/V Bay Eagle* anchor site used for part of the intensive tidal survey. These four stations were sampled four times each, except for station A, which was sampled only three times. At each station, the water column was profiled using an absorption-attenuation meter (AC9), a backscattering sensor (VSF) and a multi-parameter water quality sensor (YSI; temperature, conductivity, depth, salinity, dissolved oxygen, pH) to approximately one-half meter above the bottom. On station, the SERC vessel was located approximately 6 m down-current from the *R/V Elis Olsson* and profiles were taken concurrently. Water samples were taken from 0.5 m depth at station C during each pass across the river using a point sampler (Labline, 2 liter). Separate samples were not collected for bacterial counts during the lateral survey as had been for the axial surveys. Water samples were handled and analyzed as described above for the axial cruises. SERC did not participate in the 2005 lateral survey because it was likely that the sediment concentrations would have exceeded the operational range of the VSF in the region of the river chosen for the tidal intensive work.

*Lower Potomac River/Chesapeake Bay Cruise.* The lower Potomac River cruises involved only SERC staff. Four stations were visited using SERC's 12 m workboat, *R/V Saxatilis*, on July 26, 2005, two in the bay (CB5.2, CB5.3) and two in the Potomac (LE2.2, LE2.3); these stations coincided with those used by the Chesapeake Bay Monitoring Program. At each station, the water column was profiled using an absorption-attenuation meter (AC9) and a backscattering sensor (VSF) to approximately 9-16m depth. A multi-parameter water quality sensor (YSI) was used to collect temperature and salinity profiles to approximately 8.5-11m depth. The cable length limited the profiling depth of the YSI. In addition, the water column was profiled using a Satlantic Micropro system to approximately 10-11.5m depth. The sensors attached to the Micropro system measured upwelling radiance and downwelling irradiance in 7 wavebands (10 nm half-power): 412, 443, 490, 510, 555, 671, and 684 nm.

Water samples were collected from 1 m depth at all stations and from 4 m depth from three stations (CB5.3, LE2.2, LE2.3) using a point sampler (Labline, 2 liter); an integrated water sample was collected from station CB5.2. The water samples were filtered on board the research vessel immediately after collection for chlorophyll, particulate absorption and CDOM absorption. Filters and filtrate were transported back to the laboratory on ice. The remaining water was kept at 4ºC until analysis for absorption and attenuation coefficients, turbidity and

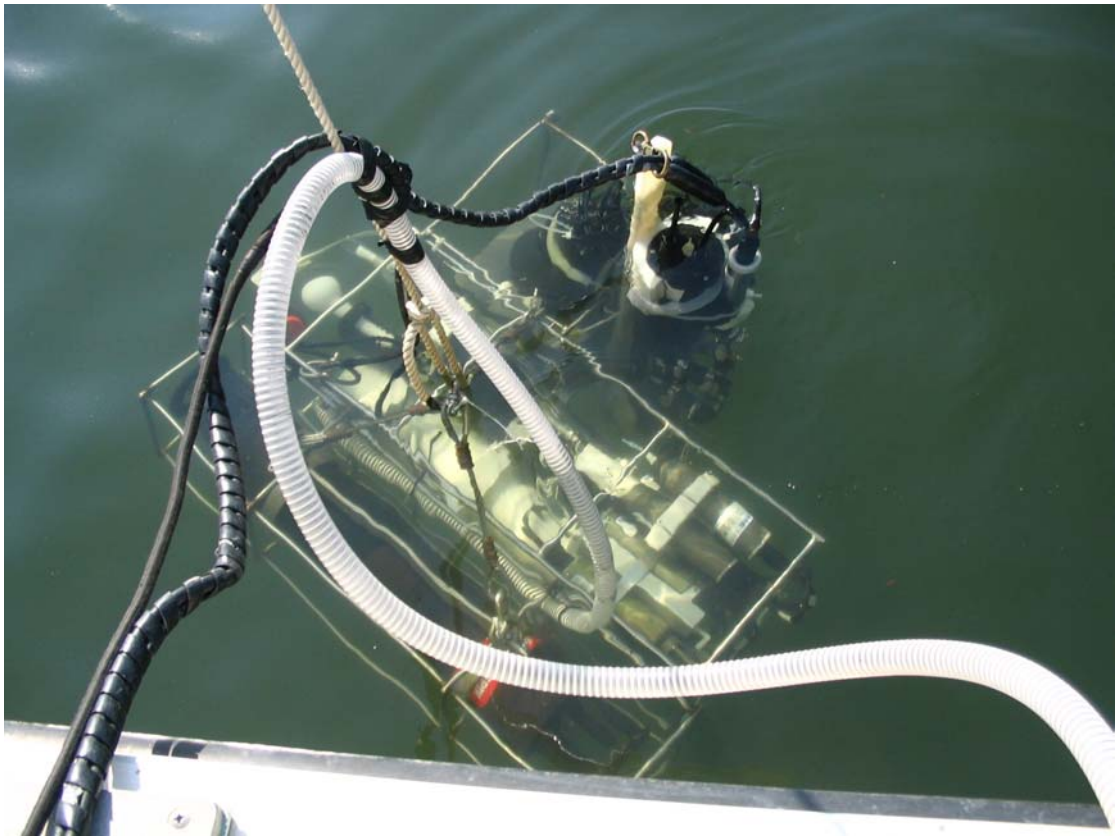

Figure 2. Instrument package used to collect vertical profiles of the water column properties. Instruments include a WETLabs absorption and attenuation meter (AC9) and backscattering meter (ECO VSF3), sensors for conductivity, temperature, depth, dissolved oxygen (YSI SBE23), scalar photosynthetically active radiation (PAR, Licor), particle-size (LISST-100), transmittance at 660 nm (10cm WETLabs Cstar transmissometer), optical backscattering turbidity (D&A OBS 3) and algal fluorescence (WETLabs WETStar).

filtration for total suspended solids at the laboratory. Additional samples were not collected for bacterial cell counts during any of the lower Potomac cruises.

*Lower Potomac/St. Marys River Cruises.* The lower Potomac and St. Marys Rivers were surveyed in September, October and November, 2005 using a SERC-owned research vessel, the *R/V Macoma*. This cruise did not include participation of VIMS or UMCES Horn Point Laboratory personnel. Four stations were visited, three in the Potomac (LE2.2, LE2.3, Piney Point) and one in the St. Marys River. The Potomac stations coincided with those used by the Chesapeake Bay Monitoring Program and Maryland Department of Natural Resources. In September, attempts were made to profile the water column using an absorption-attenuation meter (AC9) and a backscattering sensor (VSF); however, the battery did not have enough power to run all of the instruments together. Instead, the VSF was held at 1 m and then 5 m depth to collect data coinciding with water samples brought back to the laboratory. For this cruise, water samples were collected by means of a point sampler.

For the October and November cruises, the water column was profiled at each station using an absorption-attenuation meter (AC9) and a backscattering sensor (VSF) to approximately 6-13.5 m depth. A YSI multi-parameter probe was used to collect temperature and salinity profiles. Water samples were collected from 1 and 4 m depth from all four stations. On these cruises, the water collected for laboratory analyses came directly from the AC9 while the instrument was taking measurements by means of tubing connected to the outflow of the pump attached to the AC9. The flow rate was about 2 liters per minute. Water samples were handled and analyzed as described above for the axial cruises.

Analysis of Absorption Spectra.

Absorption and scattering coefficients are inherent optical properties, and therefore can be separated into contributions due to different substances. We may write

$$a_t(\lambda) = a_w(\lambda) + a_g(\lambda) + a_p(\lambda) \tag{3a}$$

where $a_t$ is the total absorption, and $a_w$, $a_g$, and $a_p$ are the absorption due, respectively, to water, chromophoric dissolved organic matter (CDOM), and particulate matter, and all are functions of wavelength, $\lambda$ (a list of frequently used notation is provided). Absorption by particulate matter can be expressed as the sum of that due to phytoplankton, $a_\phi$, and that due to all other particulates, $a_{p\text{-}\phi}$. The absorption spectrum of water is considered constant for this analysis (Pope and Fry 1997), and is subtracted from absorption measurements by the processing software for the instrument used to make the absorption measurements (see below), so we may write,

$$a_{t-w}(\lambda) = a_g(\lambda) + a_\phi(\lambda) + a_{p-\phi}(\lambda) \tag{3b}$$

where $a_{t\text{-}w}(\lambda)$ is the total absorption less that due to water.

We may express the shape of the absorption spectrum of all other constituents by normalizing the absorption at all wavelengths to the absorption at a characteristic wavelength.

Thus we define normalized absorption spectra for CDOM, phytoplankton, and non-algal particulates (NAP), respectively, as

$$g(\lambda) = \frac{a_g(\lambda)}{a_g(440)} \tag{4a}$$

$$\phi(\lambda) = \frac{a_\phi(\lambda)}{a_\phi(675)} \tag{4b}$$

and

$$p(\lambda) = \frac{a_{p-\phi}(\lambda)}{a_{p-\phi}(440)} \tag{4c}$$

where the characteristic wavelength for absorption by CDOM and NAP was chosen to be 440 nm by convention (Cuthbert and del Giorgio 1992, Kirk 1994) and 675 nm for absorption by phytoplankton because it is an absorption peak for chlorophyll.

Another characteristic of inherent optical properties is that they are proportional to the concentration of the causative parameter. By convention, the concentration of CDOM is reported directly as the absorption by filtered water at 440 nm, $a_g(440)$. For absorption by phytoplankton and non-algal particulates we may define specific absorption coefficients such that

$$a_\phi(675) = a_\phi^*(675)[CHLA] \tag{5a}$$

and

$$a_{p-\phi}(440) = a_{p-\phi}^*(440)[TSS] \tag{5b}$$

where $a_\phi^*(675)$ is the specific-absorption coefficient at 675 nm of phytoplankton chlorophyll, [CHLA], and $a_{p\text{-}\phi}^*(440)$ is the specific-absorption coefficient at 440 nm of total suspended solids, [TSS]. The wavelength designations for the specific-absorption coefficients have been dropped for notational convenience. Absorption by phytoplankton and by NAP are distinguished by using the quantitative filter pad technique, which employs solvent extraction to remove phytoplankton pigments (Kishino et al. 1985).

Analysis of Scattering Spectra

The particulate scattering spectrum, $b_p(\lambda)$,is often represented as a power function of wavelength (Boss et al. 2001),

$$b_p(\lambda) = b_p(555)\left(\frac{555}{\lambda}\right)^\eta \tag{6a}$$

where $b_p$ = particulate scattering, and $\eta$ is a spectral exponent. Small mineral particles, bacteria, viruses, and small detrital particulates are characterized by relatively high values of the scattering spectral exponent ($\eta$), 1 or higher, while nano- and micro- phytoplankton are characterized by relatively small $\eta$, <0.2. It has been shown, however, that pigment absorption by phytoplankton

cells can lead to a reduction of scattering in the pigment absorption bands (Bricaud et al. 1988). This reduction is difficult to model mechanistically, as it requires knowledge of several parameters that cannot be known a priori about a sample, e.g. size distribution and index of refraction of the phytoplankton population, and other parameters. We can represent this reduction of scattering in phytoplankton absorption bands empirically with a scalable function roughly proportional to $\phi(\lambda)$ translated to have a value of 0 at 555 nm,

$$b_p(\lambda) = b_p(555)\left[\left(\frac{555}{\lambda}\right)^{\eta} - \phi_i b_n^{\phi}(\lambda)\right] \tag{6b}$$

where $\phi_i$ is a variable scalar, and $b_n^{\phi}(\lambda)$ is an empirical function that is roughly proportional to phytoplankton absorption.

As with absorption, we can define the scattering spectral shape in terms of a normalized scattering function, $b_n(\lambda)$, by normalizing to the scattering coefficient at a characteristic wavelength, taken to be 555 nm due to its proximity to the center of the visible wavelength range,

$$b_n(\lambda) = \frac{b_p(\lambda)}{b_p(555)} = \left(\frac{555}{\lambda}\right)^{\eta} - \phi_i b_n^{\phi}(\lambda) \tag{6c}.$$

The empirical scalar depends more on the relative homogeneity of the phytoplankton size distribution than on the amount of chlorophyll present. As with absorption by NAP, the magnitude of scattering at the reference wavelength is scaled by a specific-scattering and TSS, i.e.

$$b_p(555) = b_p^*(555)[TSS] \tag{6d}$$

where $b_b^*(555)$ is the specific-scattering coefficient for TSS at 555 nm.

## Results and Discussion

Radiative Transfer Modeling.

An abbreviated example of the procedure for deriving simple expressions for relating diffuse attenuation coefficients to inherent optical properties is illustrated in Figure 3. For the specific case of *sza*=15º ($\mu_0$=0.981), *B*=0.006, and *b/a*=2.5, we simulated the profile of downwelling irradiance, $E_d(z)$ (Figure 3a). Three simulated $E_d$ less than $10^{-4}\cdot E_0$, denoted by the cyan shaded region, were omitted from further analysis for this profile. For each remaining depth we calculated the average diffuse attenuation coefficient from the surface to depth $z$ as $K_d(z) = -\frac{1}{z}\ln\left[\frac{E_d(z)}{E_d(0)}\right]$ (Figure 3b, red squares), and $\kappa_z$ by rearrangement of equation (2) (Figure 3b, black circles).

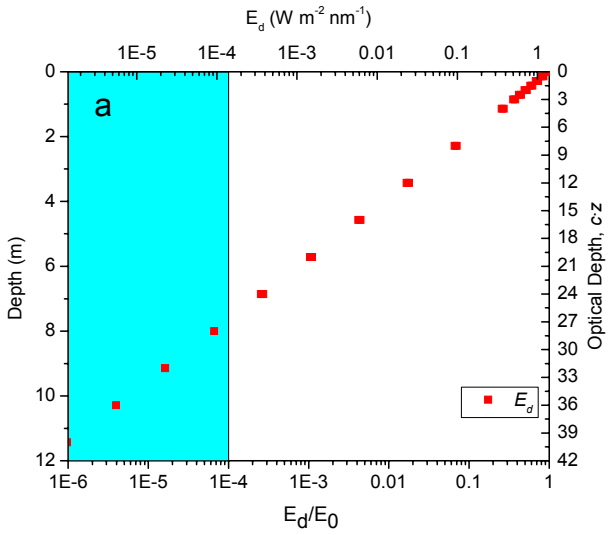


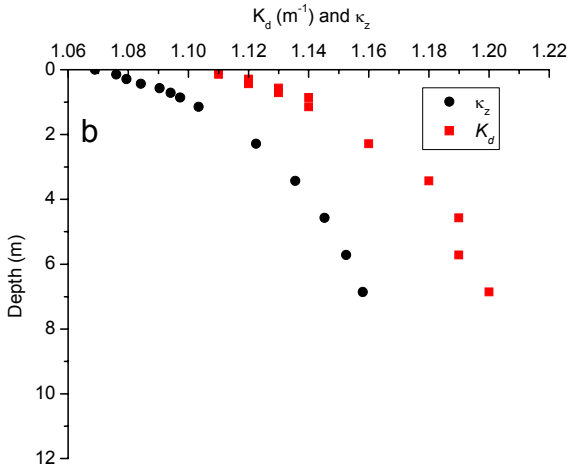


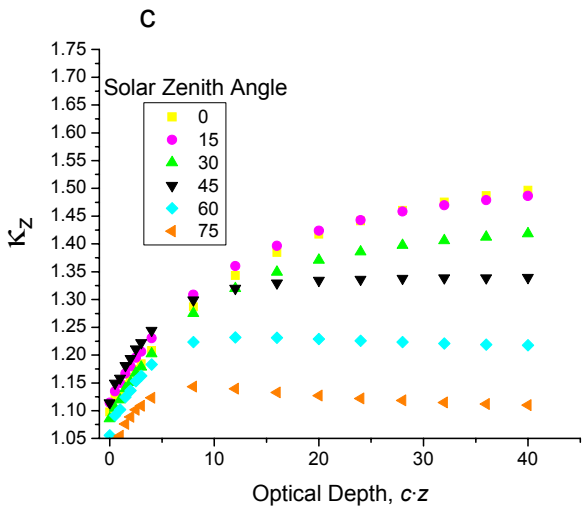


Figure 3. Example of procedure for deriving simple expressions for relating diffuse attenuation coefficients to inherent optical properties. a) Simulated profile of downwelling irradiance, $E_d(z)$, for the specific case of *sza*=15º (μ0=0.981), *B*=0.006, and *b/a*=2.5. Three simulated $E_d$ less than $10^{-4} \cdot E_0$, denoted by the cyan shaded region, were omitted from further analysis for this profile. b) Calculated average diffuse attenuation coefficient (red squares) and coefficient $\kappa_z$ (black circles). c) $\kappa_z$ versus optical depth for varying solar zenith angles.

For each profile, $\mu_0$, $B$, and $b/a$ remain fixed while $\Gamma$ varies. Therefore we first proceeded to eliminate the $\Gamma$ dimension by parametric curve fitting. Generally, $\kappa_z$ initially increased with increasing optical depth, sometimes to an asymptote, and other times to a maximum from which it then declined, depending on the value of other parameters (Figure 3c). We reduced the $\Gamma$ dimension by fitting $\kappa_z$ to the empirical equation,

$$\kappa_z = \kappa_0 + \kappa_s \left( \frac{\Gamma}{\Gamma + K_\Gamma} \right) \left(1 - \beta_\Gamma \Gamma\right) \tag{7}$$

where $\kappa_0$, $\kappa_s$, $K_\Gamma$, and $\beta_\Gamma$ are empirical parameters that now must be fit in terms of the remaining dimensions, $\mu_0$, $B$, and $b/a$. Remaining dimensions were reduced in the order $b/a$, $B$, then $\mu_0$. Complete equations are given in Table 2, representing the order in which they were derived. Operationally the equations are solved in the reverse order of Table 2.

The fit of the set of equations in Table 2 are compared with the data used to derive them (black squares) as well as independently generated data (red circles) in Figure 4a. Although some positive bias develops at very high $K_d$ (>4 $m^{-1}$), the simplified empirical model performs well at most commonly observed values. The predicted spectrum of $K_d$ agrees well in shape and overall magnitude with that calculated by *Hydrolight*, using the same water quality concentrations and mass-specific absorption and scattering coefficients (Figure 4b). Similarly, the empirical model correctly represents the depth dependence of $K_d$ for monochromatic light, showing an increase to an asymptotic value due to the change in radiance distribution from direct to diffuse as depth increases (Figure 4c). Starting from the same depth profile as in Figure 4c, varying the backscatter fraction over its expected range from 0.006 to 0.036 results in a variation in monochromatic $K_d$ from 1.2 to 1.52 $m^{-1}$ (Figure 4d, circles), while varying the solar zenith angle (*sza*, which controls $\mu_0$) from 0 to 75° changes $K_d$ from 1.35 to 1.58 $m^{-1}$ (Figure 4d, triangles). Based on these comparisons, we conclude that our ability to specify spatial and temporal variability in the inherent optical properties, particularly specific-absorption coefficients, specific-scattering coefficients, and backscattering fraction, will be the limiting factor in the accuracy of predictions of the empirical simplification derived from *Hydrolight* simulations.

## Potomac River Optical Properties

*Absorption by CDOM*. The spectral shape of absorption by CDOM conformed well to a negative exponential (Figure 5a) represented by,

$$a_g(\lambda) = a_g(440)\exp\left[-s_g(\lambda - 440)\right] \tag{30}$$

where the spectral slope of absorption, $s_g$, varied from 0.009 to 0.022 and averaged 0.0167 $nm^{-1}$. General linear model (GLM) analysis indicated that $s_g$ varied only weakly with station (P=0.06) increasing in the upstream direction to an apparent peak around km 30, and then decreasing again (Figure 5b). $s_g$ varied more strongly with month ($P<10^{-4}$), decreasing from 0.0193 $nm^{-1}$ in March, to 0.0185 $nm^{-1}$ in June, to 0.0127 $nm^{-1}$ in August. The weak variation with station was in part due to the limited number of sampling trips (3). $s_g$ decreased with increasing $a_g(440)$ (Figure 5c), consistent with the observation that the processes that remove CDOM operate

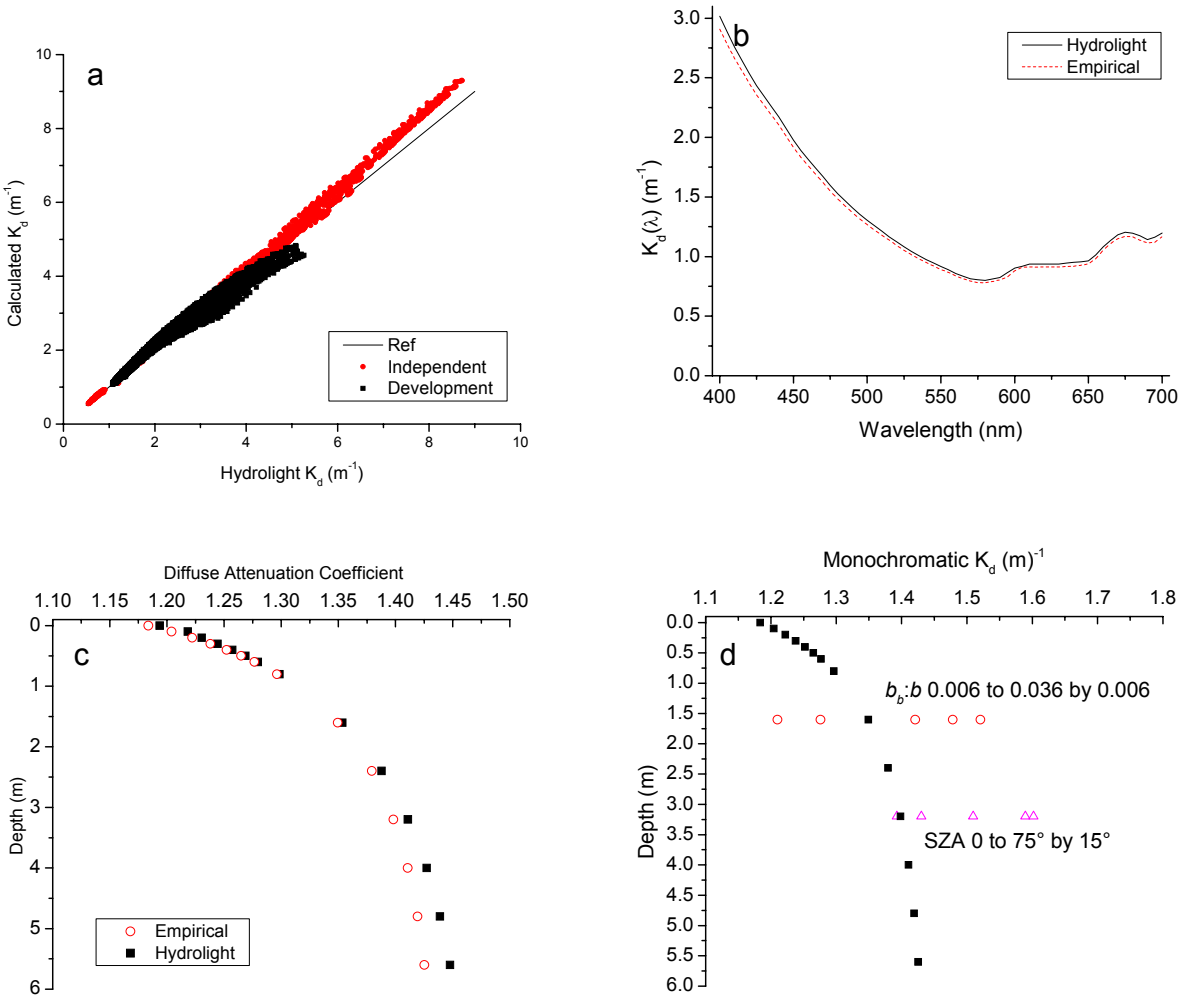


Figure 4. Radiative transfer modeling results. a) Diffuse attenuation coefficients from the simplified empirical model compared with the data used to derive the model (black squares) as well as independently generated data (red circles). b) Spectrum of the diffuse attenuation coefficient calculated by the empirical simplification (red dashed line) and by *Hydrolight* (solid black line). c) Depth dependence of the diffuse attenuation coefficient for monochromatic light calculated by the empirical model (red circles) and by *Hydrolight* (black squares) . d) Sensitivity of the diffuse attenuation coefficient for monochromatic light to changes in the backscatter fraction from 0.006 to 0.036 (red circles). The pink triangles similarly show changes resulting from varying the solar zenith angle from 0 to 75°. The black squares show the same depth profile as in c for reference.

preferentially on the longer wavelength-absorbing compounds (Vodacek et al. 1997). We fit $s_g$ by a line,

$$s_g = \max\left[0.0228 - 0.00741 a_g(440), 0.01\right] \tag{31}$$

which is bounded below at 0.01 $nm^{-1}$ to prevent unrealistic values when used with CDOM concentrations higher than those encountered in model development.

Table 2. Equations for calculating the diffuse attenuation coefficient for downwelling light from inherent optical properties (IOPs), $a$, $b$, and $b_b$, and boundary conditions $\mu_0$, and optical depth, $\Gamma$.

| Dependence | Equation | Number |
|---|---|---|
| IOPs | $K_d = \kappa_z \dfrac{a + b_b}{\mu_0}$ | (8) |
| $\Gamma$ | $\kappa_z = \kappa_0^\Gamma + \kappa_s^\Gamma \dfrac{\Gamma}{\Gamma + K_\Gamma}\left(1 - \beta_\Gamma \Gamma\right)$ | (9) |
| $b/a$ | $\kappa_0^\Gamma = p_1^\varpi + p_2^\varpi \dfrac{b/a}{b/a + p_3^\varpi}\left(1 - p_4^\varpi\, b/a\right)$ | (10) |
| $b/a$ | $K_\Gamma = q_1^\varpi + q_2^\varpi \kappa_s^\Gamma$ | (11) |
| $b/a$ | $\kappa_s^\Gamma = q_3^\varpi \dfrac{b/a}{b/a + q_4^\varpi}$ | (12) |
| $B$ | $p_1^\varpi = \dfrac{g_1^\mu}{\sqrt{1 + \left(g_2^\mu B\right)^2}}$ | (13) |
| $B$ | $p_2^\varpi = \dfrac{f_1^B}{\tan^{-1}\left(f_2^B B\right)}$ | (14) |
| $B$ | $p_3^\varpi = f_3^B \exp\left(-\dfrac{B}{f_4^B}\right) + f_5^B$ | (15) |
| $B,\ \mu_0$ | $p_4^\varpi = 0.003277 + \left(1.23042\mu_0 - 0.33809\right)B$ | (16) |
| $B$ | $q_1^\varpi = s_1^B q_3^\varpi + s_2^B$ | (17) |
| $B$ | $q_2^\varpi = t_1^B q_3^\varpi + t_2^B$ | (18) |
| $B$ | $q_4^\varpi = r_1^B q_3^\varpi + r_2^B$ | (19) |
| $B$ | $q_3^\varpi = q_1^B \exp\left(-B/q_2^B\right) + q_3^B$ | (20) |

$$\mu_0 \qquad q_1^B = 173.0513\mu_0^2 - 262.586\mu_0 + 100.4864 \tag{21}$$

$$\mu_0 \qquad q_2^B = -0.06895\mu_0^2 + 0.104437\mu_0 - 0.02974 \tag{22}$$

$$\mu_0 \qquad q_3^B = 6.917277\mu_0^2 - 9.04774\mu_0 + 3.236307 \tag{23}$$

$$\mu_0 \qquad r_1^B = 230.4608\mu_0^2 - 543.805\mu_0 + 331.4226 \tag{24}$$

$$\mu_0 \qquad r_2^B = 87.9354\mu_0^2 - 142.658\mu_0 + 41.31318 \tag{25}$$

$$\mu_0 \qquad s_1^B = -54.6704\mu_0^2 + 90.12786\mu_0 - 35.549 \tag{26}$$

$$\mu_0 \qquad s_2^B = 51.435\mu_0^2 - 75.6922\mu_0 + 28.40758 \tag{27}$$

$$\mu_0 \qquad t_1^B = -144.148\mu_0^2 + 205.3784\mu_0 - 56.5336 \tag{28}$$

$$\mu_0 \qquad t_2^B = 166.7199\mu_0^2 - 261.492\mu_0 + 97.77373 \tag{29}$$

---

The overall magnitude of absorption by CDOM, as indicated by the scalar in Eq. 30, $a_g(440)$, was generally erratic in the spatial dimension (Figure 5d); by far the strongest variation of $a_g(440)$ was with season, increasing from March through late summer (Figure 5d). The late summer maximum in $a_g(440)$ is out of phase with the monthly average seasonal flow of the Potomac River (Figure 6a). As a consequence, the relationship between $a_g(440)$ and salinity is very weak for the Potomac (Figure 6b). This relationship could result from either in situ seasonal production of CDOM from decaying phytoplankton, vascular plants, and decomposing organic matter from the bottom, or from point source inputs that are less diluted by flow in the late summer.

*Absorption by Chlorophyll*. Due to high concentrations of suspended sediment, and occasionally low chlorophyll concentrations, the shape of the chlorophyll absorption spectrum was sometimes difficult to measure in samples from the tidal freshwater Potomac. At low chlorophyll concentrations, the residual spectrum after subtraction of methanol-extracted absorption measurements sometimes included negative values (Figure 7a, solid line). At high concentrations of TSS the residual spectrum was often strongly peaked in the blue (Figure 7a, dashed line), signifying some extraction of NAP color by methanol treatment (Gallegos 2005). Screening the measurements for samples meeting the criteria, [CHLA]>10 mg $m^{-3}$ and TSS<20 g $m^{-3}$ produced a realistic normalized chlorophyll absorption spectrum, based on 36 measurements meeting the criteria (Figure 7b, error bars are ±1 standard error).

Phytoplankton absorption at the reference wavelength, 675 nm, was generally proportional to chlorophyll concentration (Figure 7c). Several measurements fell well above the central tendency of points, but the number of such outliers was relatively small, and they were left in the estimation of chlorophyll-specific absorption coefficient at 675 nm, which was 0.0223 $m^2$ (mg Chl)$^{-1}$ (Figure 7c, solid line). Measurements from one cruise during a *Microcystis* bloom

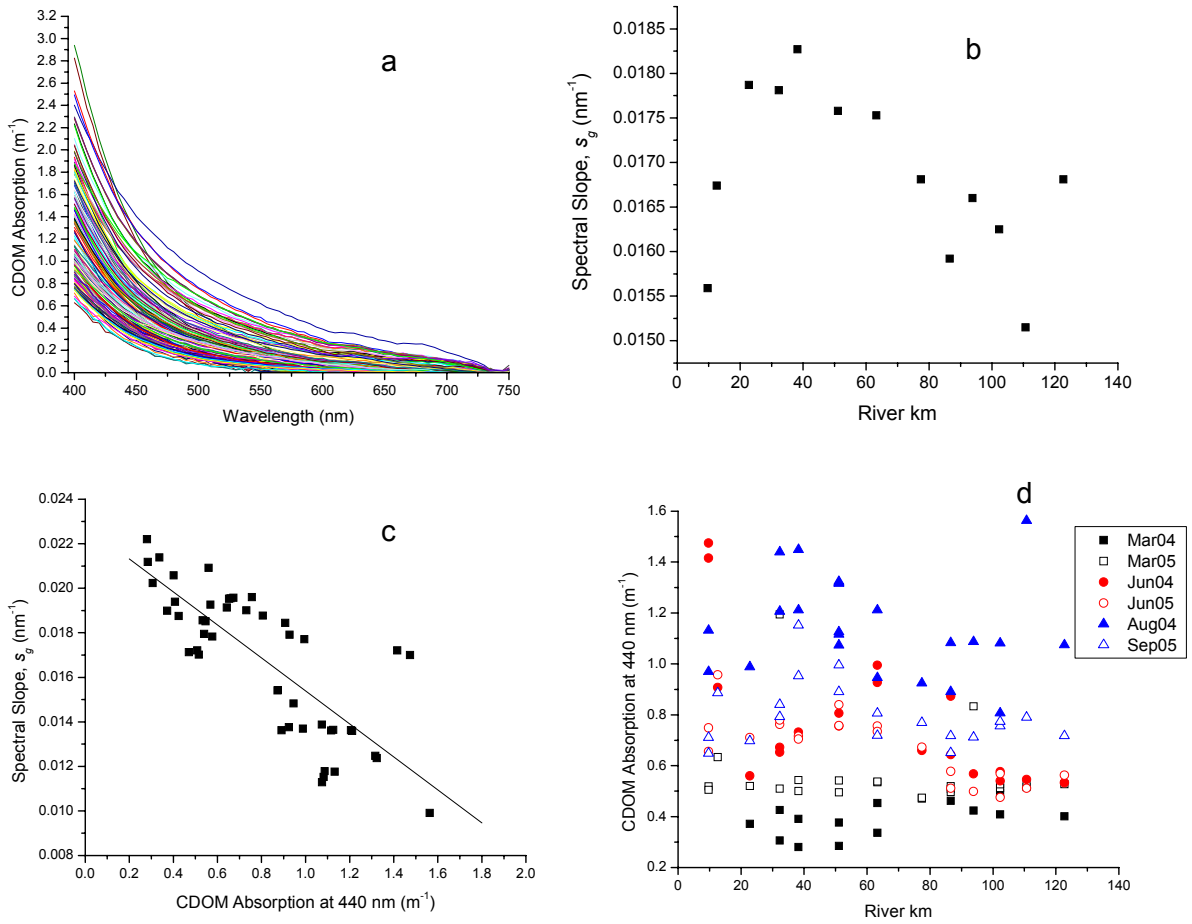


Figure 5. Absorption by colored dissolved organic matter (CDOM) for the Potomac River. a) Absorption spectra for all samples. b) Mean spectral slope versus river kilometer. c) Spectral slope versus CDOM absorption at 440 nm. Fitted line is calculated by equation 31. d) Variation in CDOM absorption at 440 nm with river kilometer and season. Like symbols represent the same season.

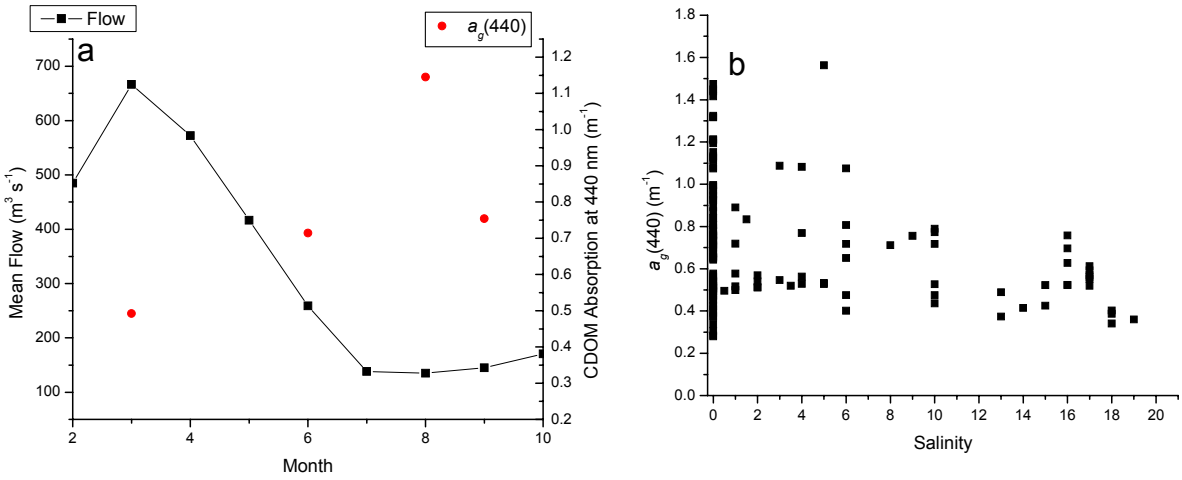


Figure 6. Colored dissolved organic matter (CDOM) source and dilution. a) Monthly averaged flow of the Potomac River (line and squares) is out of phase with seasonal mean CDOM absorption at 440 nm (red circles). b) CDOM absorption at 440 nm versus salinity indicates that salinity is not a good predictor of CDOM for the Potomac.

in June 2004, fell entirely above the estimated line, but the pattern was not repeated in 2005, so there was no strong indication of seasonality.

*Absorption by Non-algal Particulates*. The absorption spectrum of non-algal particulates, $a_{p\text{-}\phi}(\lambda)$, exhibited the typical negative exponential shape, though a minor shoulder was often apparent at about 500 nm (Figure 8a), as observed elsewhere (Bowers and Binding 2006). The spectral slope of NAP absorption, $s_p$, ranged from 0.0044 to 0.012 $nm^{-1}$. The average value of $s_p$ was 0.0088 $nm^{-1}$, and >85% of values fell between 0.008 and 0.010 $nm^{-1}$ (Figure 8b). Similar to the spectral slope of CDOM absorption, $s_p$ varied inversely with the overall magnitude of NAP absorption (Figure 8c), though the relationship was more scattered than that of $s_g$ vs. $a_g(440)$ (cf. Figures 8c, 5c). We estimated $s_p$ by

$$s_p = 0.00768 + 0.002514 \exp\left[-a_{p-\phi}(440)/1.1808\right] \tag{32}$$

where $a_{p\text{-}\phi}(440)$ is estimated by equation 33b below.

The magnitude of absorption at the reference wavelength, 440 nm, was linearly related to the concentration of TSS (Figure 9a). There was, however, a significantly positive intercept, which is problematic because it implies that there is absorption by particulate matter when the TSS concentration is zero. Aside from defying principles of conservation of energy, inclusion of an intercept term in modeling relationships has undesirable ramifications for management decisions, because the full benefit of TSS reduction would not be predicted at low concentrations. As an alternative representation we plotted the specific-absorption coefficient of NAP calculated on a sample-by-sample basis, i.e. $a^*_{p-\phi}(440) = \dfrac{a_{p-\phi}(440)}{[TSS]}$, against TSS (Figure 9b). Calculated in this way, $a_{p\text{-}\phi}^*(440)$ declined asymptotically to a stable value of about 0.067

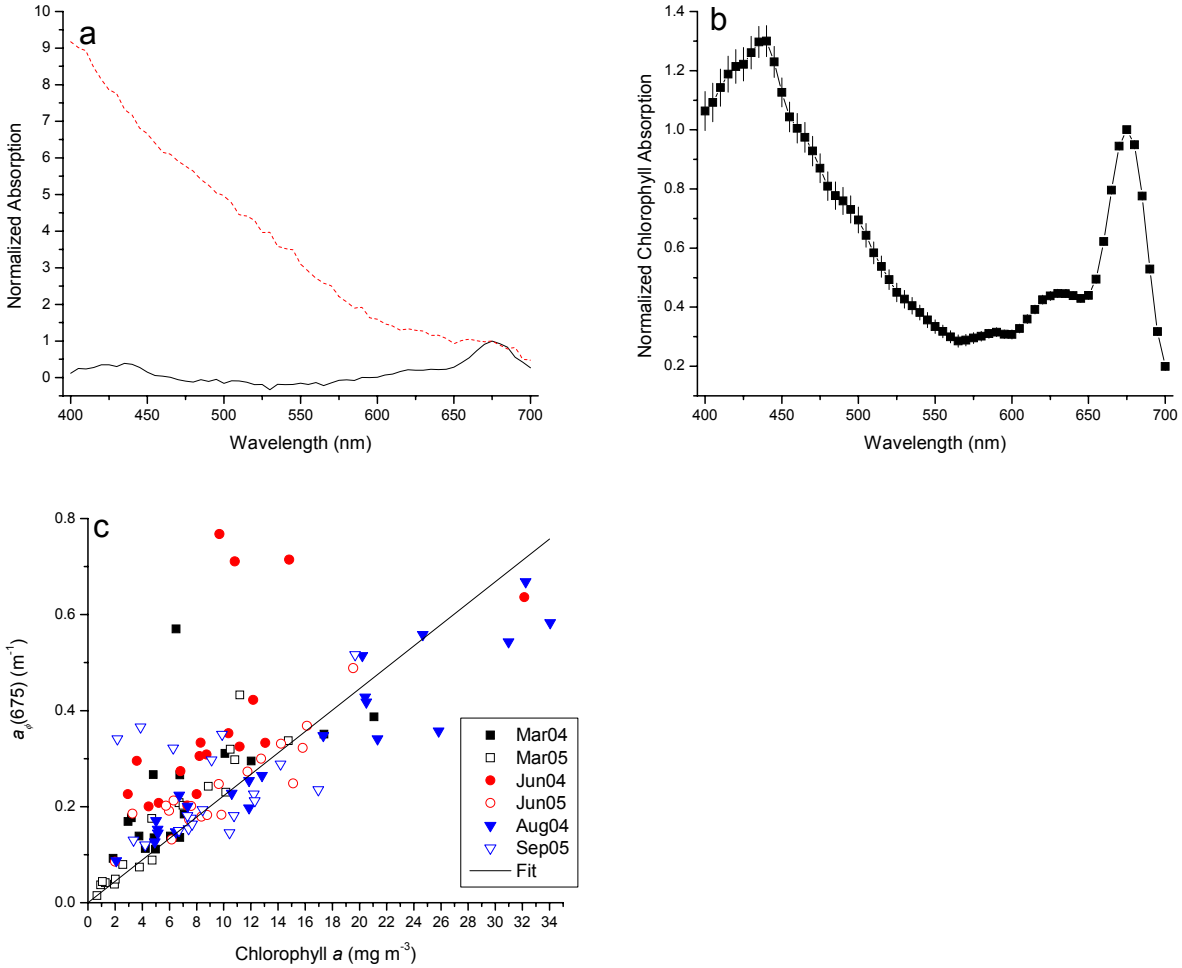


Figure 7. Absorption by chlorophyll. a) Problems encountered in measuring the chlorophyll absorption spectrum in the presence of high concentrations of TSS. Methanol-extracted particulate absorption was unrealistically sloped in the blue (dashed line) when non-algal particulate color was extracted, or produced negative estimates (solid line) when chlorophyll was low and TSS was high. b) Normalized chlorophyll absorption spectrum for samples meeting the criteria, [CHLA]>10 mg m$^{-3}$ and TSS<20 g m$^{-3}$. Error bars are ±1 standard error, n=36. c) Phytoplankton absorption at 676 nm versus chlorophyll *a* concentration. The estimated chlorophyll-specific absorption coefficient at 676 nm, which was 0.0223 m$^2$ (mg Chl)$^{-1}$, is shown by the solid line. Like symbols represent the same season.

$m^2\ g^{-1}$. By least squares minimization, we estimated the specific-absorption coefficient of NAP as

$$a^*_{p-\phi}(440) = 0.075 + 0.400 * \exp(-TSS/2.662) \quad (33a),$$

so that absorption at the reference wavelength is calculated as

$$a_{p-\phi}(440) = TSS[0.075 + 0.400 * \exp(-TSS/2.662)] \quad (33b).$$

The fit of equation 33b to measured NAP absorption at 440 nm is unbiased (Figure 9c), and equation 33b has a zero intercept at TSS=0 g $m^{-3}$. The nonlinearity in equation 33b primarily affects predictions only for TSS<10 g $m^{-3}$.

*Scattering*. In response to the wide range of observed TSS concentrations, scattering coefficients ranged from <2 to >120 $m^{-1}$ (Figure 10a). Although scattering spectra appeared relatively featureless when plotted on a common scale, normalizing to $b_p(555)$ revealed considerable variety in spectral shape (Figure 10b).

Scattering spectra were well represented by equation 6c. Fits to measured spectra with the highest η and highest $\phi_i$ are shown in Figure 10c. Overall, η ranged from -0.0304 to 0.868 (Figure 10c, black line) and averaged 0.502. $\phi_i$ ranged from 0.0077 to 0.175 (Figure 10c, red dashed line) and averaged 0.0714. The inset to Figure 10c illustrates the basis functions scaled in equation 6c to produce the final fit to the scattering spectrum. The empirical values of $b^{\phi}_n(\lambda)$ are given below in Table 3. The spectral exponent, η, varied significantly with station location (Figure 10d), showing a local minimum between ca. 30 to 50 km below the fall line. A lower spectral exponent could be characteristic of particle populations consisting or greater percentage of organic particulates, or a larger diameter inorganic particles than those in either direction up or down estuary. In spite of these patterns, in the interest of parsimony, these parameters will be fixed at their averages in the model, and sensitivity to variations will be examined later.

The magnitude of scattering at the reference wavelength, 555 nm, was linearly related to TSS (Figure 11a). As with non-algal absorption, there was a positive intercept of about 3.5 $m^{-1}$ on the scattering axis. For the same reasons indicated above for $a_{p-\phi}(440)$, an intercept at zero concentration has undesirable properties in a model. The specific-scattering coefficient calculated on a sample-by-sample basis as $b_p^*(555) = \dfrac{b_p(555)}{TSS}$ exhibited a similar pattern with TSS as non-algal particulate absorption (Figure 11b), and was fit by the equation

$$b^*_p(555) = 0.5617 + 1.7377\exp(-TSS/5.288) \quad (34a),$$

so that scattering at 555 nm is represented as

$$b_p(555) = TSS[0.5617 + 1.7377\exp(-TSS/5.288)] \quad (34b).$$

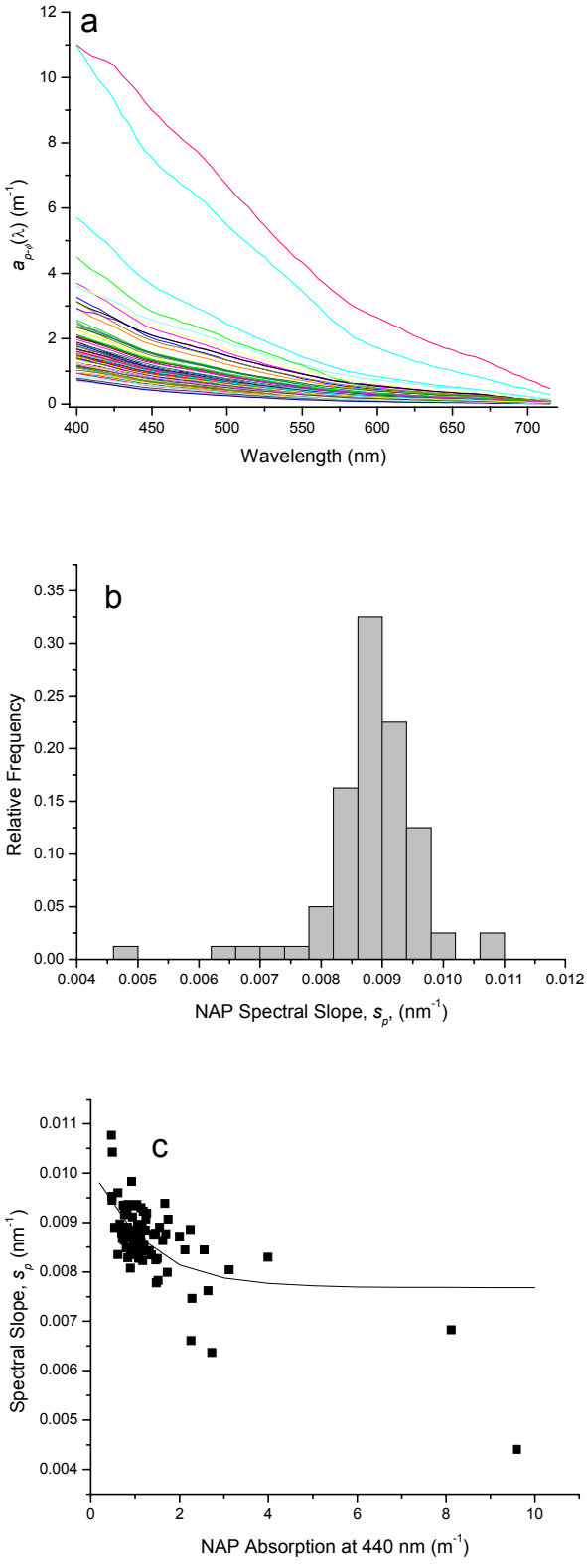


Figure 8. Absorption by non-algal particulates (NAP). a) Non-algal particulate absorption spectra. b) Histogram of NAP spectral slopes. c) Spectral slope versus NAP absorption at 440 nm. Solid line is calculated by equation 32.

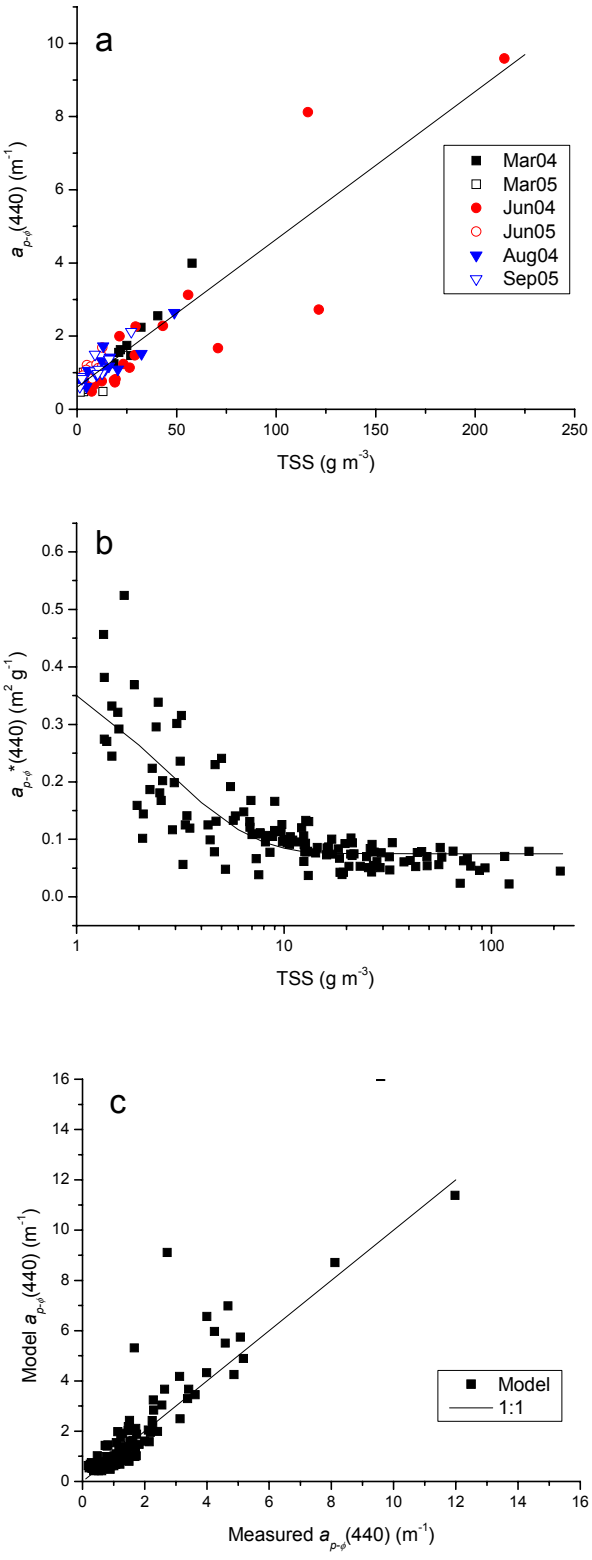


Figure 9. Relationship of non-algal particulate (NAP) absorption to total suspended solids (TSS). a) Linear relationship between NAP absorption at 440 nm and TSS. Like symbols represent the same season. b) Specific-absorption coefficient of NAP calculated on a sample-by-sample basis versus TSS. Solid line is calculated by equation 33a. c) Modeled (equation 33b) versus measured NAP absorption at 440 nm. See text for further discussion.

The fit of equation 34b to measured $b_p(555)$ is unbiased (Figure 11c), and equation 34b has a zero intercept at TSS=0 g $m^{-3}$. As for NAP absorption, the nonlinearity in equation 34b primarily affects predictions only for TSS<10 g $m^{-3}$.

*Backscattering*. Backscattering measurements were difficult to make on the Potomac River because the high suspended sediment concentrations encountered frequently exceeded the dynamic range of the ECO-VSF3 used to make the measurements. For 43 profiles, measurements at all 3 wavelength were within range for the instrument (Figure 12a). In nearly every case, backscattering fractions varied in the rank order $B_{430}>B_{532}>B_{650}$ (Figure 12a).

Measurements were most frequently available for the green (532 nm) sensor than for the blue or red; moreover, there were no cases in which there were readings from either the blue or red sensor without a reading from the green sensor. We can, therefore, increase our number of readings available for analysis by considering only the green sensor, for which there were 62 total measurements. There was a significant (P=0.026) decreasing trend in $B_{532}$ with distance from the fall line (Figure 12b), with the exception of a single measurement at the most upstream profile station, PR13, which declined from those stations immediately downstream (Figure 12b). The strength of the relationship is limited by the number of observations at each station, given above the points in Figure 12b. There was also a relationship between $B_{532}$ and TSS (Figure 12c), which we estimated by the empirical fit,

$$B_{532} = 0.005734 + 0.018615\exp\left(-TSS/6.5294\right) \quad (35).$$

Table 3. Values for the normalized absorption function of phytoplankton, $\phi(\lambda)$, and the empirical function $b^{\phi}_{n}(\lambda)$ that is scaled in equation 6c to represent the effect of depression scattering in phytoplankton absorption bands. $\lambda$= wavelength of light (nm).

| $\lambda$ | $\phi(\lambda)$ | $b_n^{\phi}(\lambda)$ | $\lambda$ | $\phi(\lambda)$ | $b_n^{\phi}(\lambda)$ | $\lambda$ | $\phi(\lambda)$ | $b_n^{\phi}(\lambda)$ |
|---|---|---|---|---|---|---|---|---|
| 400 | 1.06316 | 1.227376 | 550 | 0.081732 | 0.33424 | 700 | 0.19962 | 0.278689 |
| 405 | 1.09211 | 1.199041 | 555 | 0.07617 | 0.31773 | 705 | 0 | 0.233599 |
| 410 | 1.14232 | 1.165859 | 560 | 0.073768 | 0.29978 | 710 | 0 | 0.178813 |
| 415 | 1.18784 | 1.128433 | 565 | 0.074432 | 0.2854 | 715 | 0 | 0.113543 |
| 420 | 1.21412 | 1.087343 | 570 | 0.078047 | 0.28832 | | | |
| 425 | 1.22164 | 1.043145 | 575 | 0.084474 | 0.29545 | | | |
| 430 | 1.2609 | 0.996374 | 580 | 0.093552 | 0.30186 | | | |
| 435 | 1.29664 | 0.947539 | 585 | 0.105095 | 0.31025 | | | |
| 440 | 1.29989 | 0.897127 | 590 | 0.118894 | 0.31525 | | | |
| 445 | 1.22945 | 0.845602 | 595 | 0.134719 | 0.3083 | | | |
| 450 | 1.12609 | 0.793405 | 600 | 0.152315 | 0.3076 | | | |
| 455 | 1.04321 | 0.740954 | 605 | 0.171404 | 0.32762 | | | |
| 460 | 1.00487 | 0.688642 | 610 | 0.191685 | 0.3597 | | | |
| 465 | 0.97429 | 0.636841 | 615 | 0.212833 | 0.39234 | | | |
| 470 | 0.92811 | 0.585898 | 620 | 0.234502 | 0.42512 | | | |
| 475 | 0.86984 | 0.53614 | 625 | 0.25632 | 0.43791 | | | |
| 480 | 0.80926 | 0.487866 | 630 | 0.277895 | 0.44648 | | | |

| | | | | | | | | |
|---|---|---|---|---|---|---|---|---|
| 485 | 0.77725 | 0.441357 | 635 | 0.298809 | 0.44591 | | | |
| 490 | 0.75925 | 0.396866 | 640 | 0.318622 | 0.4391 | | | |
| 495 | 0.73036 | 0.354626 | 645 | 0.336871 | 0.42905 | | | |
| 500 | 0.69485 | 0.314846 | 650 | 0.35307 | 0.43981 | | | |
| 505 | 0.64304 | 0.277712 | 655 | 0.366708 | 0.49446 | | | |
| 510 | 0.58357 | 0.243386 | 660 | 0.377253 | 0.62181 | | | |
| 515 | 0.53718 | 0.212008 | 665 | 0.38415 | 0.79563 | | | |
| 520 | 0.49283 | 0.183693 | 670 | 0.386819 | 0.94484 | | | |
| 525 | 0.44998 | 0.158535 | 675 | 0.384657 | 1 | | | |
| 530 | 0.42692 | 0.136604 | 680 | 0.377039 | 0.949 | | | |
| 535 | 0.40473 | 0.117946 | 685 | 0.363317 | 0.77584 | | | |
| 540 | 0.38191 | 0.102585 | 690 | 0.342819 | 0.52889 | | | |
| 545 | 0.35622 | 0.090522 | 695 | 0.314849 | 0.31764 | | | |

*Particle Color Index, PCI*. In order to use the overall approach used here at large geographic scales, we introduce one additional parameter designed to aid in the prediction of absorption by NAP. We call the parameter the particle color index, PCI, and define it as the ratio of NAP absorption at 440 nm to particulate scattering at 555 nm,

$$PCI = \frac{a_{p-\phi}(440)}{b_p(555)} \tag{36}.$$

Highly colored sediments, such as those rich in iron oxides (Babin and Stramski 2004) or reduced muds, should have a relatively high PCI, whereas weakly absorbing quartz should have relatively lower indices. The advantage of this parameter is that it varies over a somewhat smaller range than $a_{p\text{-}\phi}^*(440)$. For example, the North River, North Carolina, is a macrotidal system with coarse sands for bottom sediments. Consequently, the specific-absorption coefficient of NAP is about an order of magnitude lower than that of TSS for the Potomac River (Figure 13a), whereas the PCI for the North River, NC, is lower than that of the Potomac by about a factor of 3 (Figure 13b). We expect that we will be able to parameterize the wider Chesapeake region more easily by measuring or estimating $b_p^*(555)$ and PCI.

Light Attenuation Model

*Summary of the model equations*. The foregoing development provides the information needed to model the inherent optical properties from water quality concentrations, and the diffuse attenuation coefficient from the inherent optical properties (Table 2). The total absorption spectrum is given by

$$a_t(\lambda) = a_w(\lambda) + a_g(440)\exp\left[-s_g(\lambda - 440)\right] + a_\phi^*(675)[CHLA]\phi(\lambda) + a_{p-\phi}^*(440)[TSS]\exp\left[-s_p(\lambda - 440)\right] \tag{37}.$$

Coefficients, $s_g$, $s_p$, $a_{p\text{-}\phi}^*(440)$, and $a_\phi^*(675)$ are given, respectively, by equations 31, 32, 33a, and the value 0.023 $m^2$ (mg Chl)$^{-1}$, *which are site-specific for the Potomac River*. Bay-wide extrapolation of the model will require values for these coefficients on a segment-by-segment

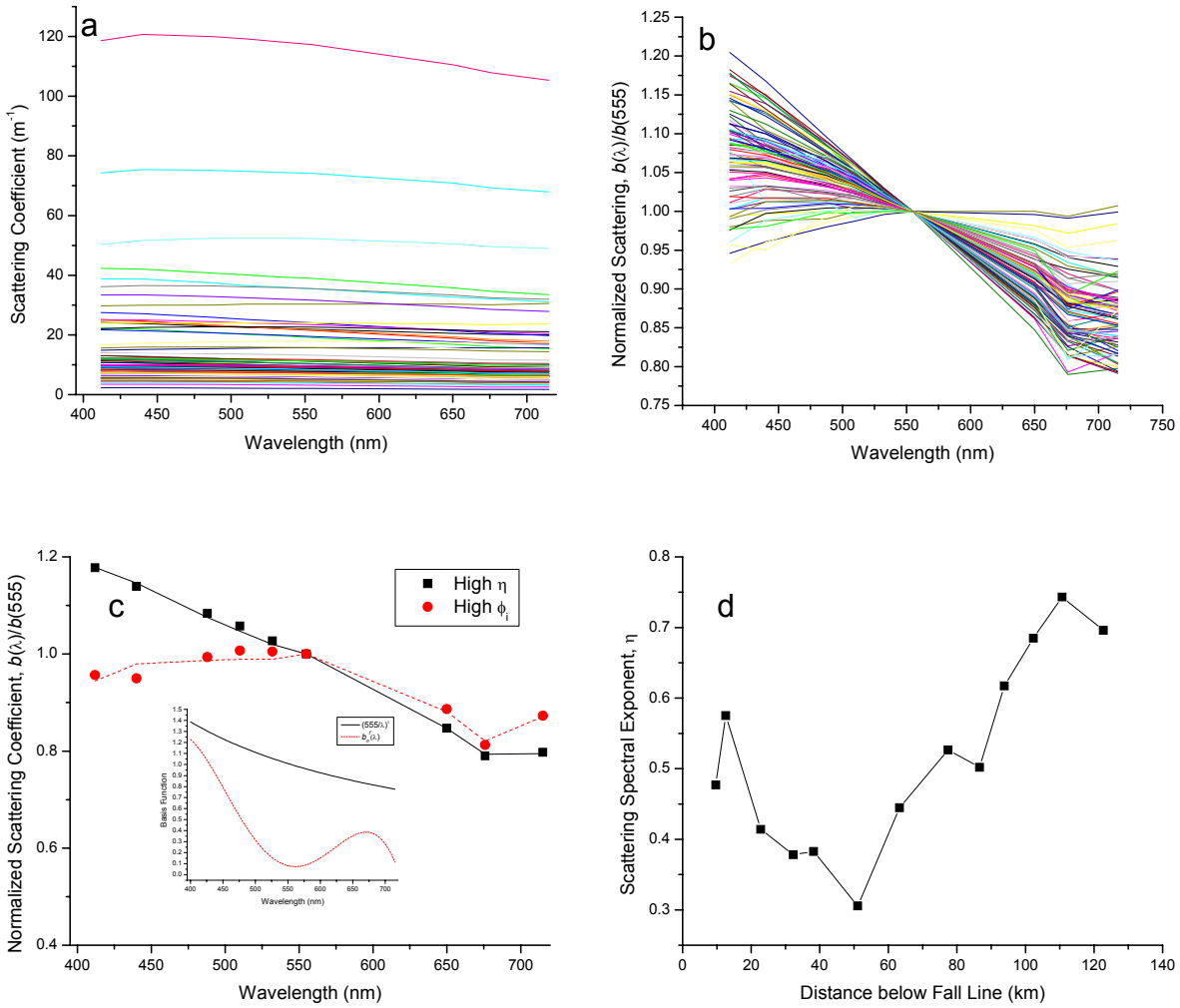


Figure 10. Scattering. a) Scattering spectra for all samples. b) Scattering spectra normalized to measured value at 555 nm. c) Fits of equation 6b to measured normalized scattering coefficient for spectra with the highest spectral exponent, $\eta$ (solid line, black squares) and with the highest scalar, $\phi_i$, that quantifies the suppression of scattering in algal absorption bands (dashed line, red circles). The inset illustrates the basis functions

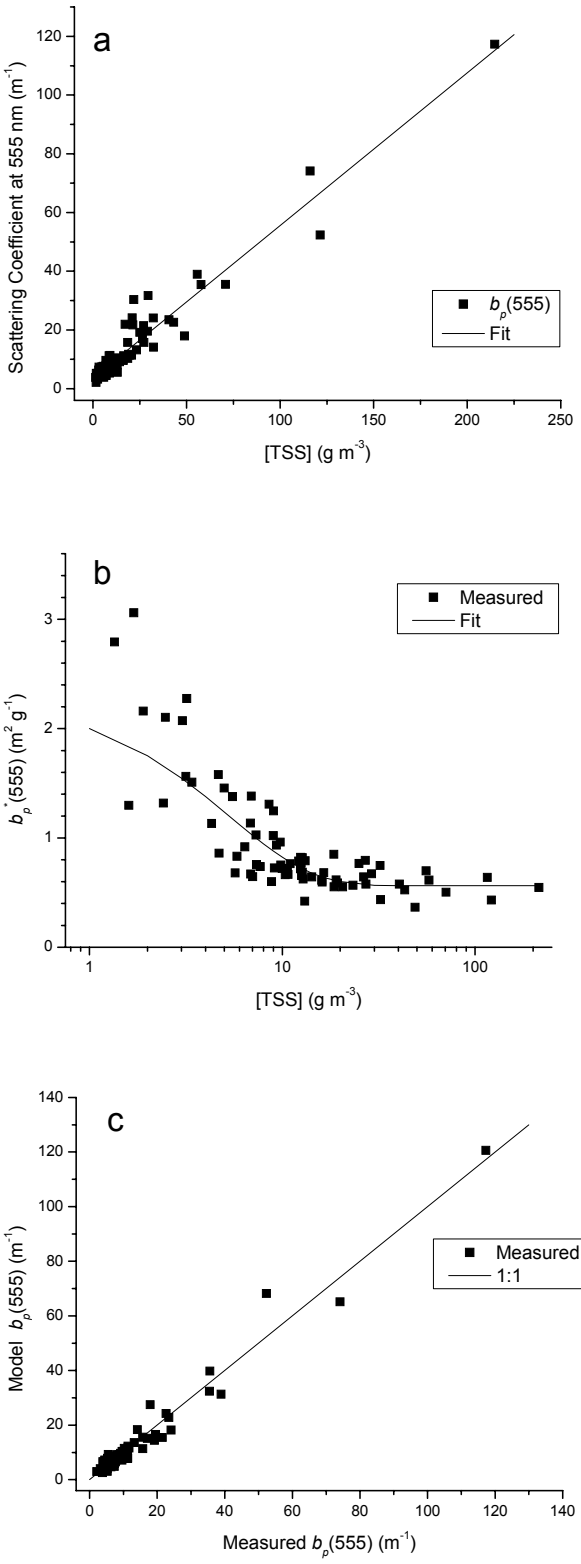


Figure 11. Relationship of scattering to total suspended solids (TSS). a) Linear relationship between the scattering coefficient at 555 nm and TSS concentration. b) Specific-scattering coefficient calculated on a sample-by-sample basis versus TSS concentration. Solid line is calculated by equation 34a. c) Modeled (equation 34b) versus measured scattering coefficient at 555 nm. See text for further discussion.

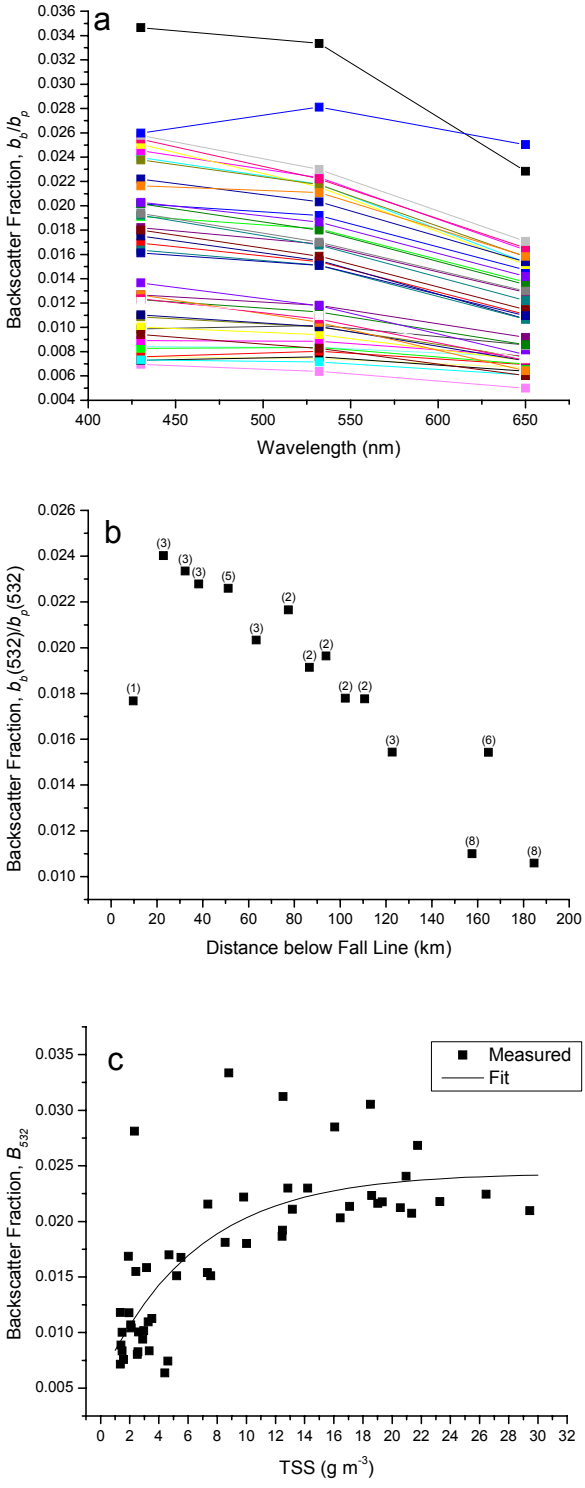


Figure 12. Backscattering. a) Backscatter fraction for 43 profiles within instrument range. b) Backscatter fraction for 62 measurements of the green (532 nm) sensor versus river kilometer. The numbers above the points are the number of observations available per station. c) Relationship between the backscatter fraction at 532 nm and total suspended solids (TSS). The solid line is estimated by empirical fit (equation 35).

basis (see below), though we expect that a single function for spectral shape of phytoplankton absorption, $\phi(\lambda)$ (Table 3) will be adequate.

The particulate scattering spectrum is given by

$$b_p(\lambda) = b_p^*(555)[TSS]\left[\left(\frac{555}{\lambda}\right)^{\eta} - \phi_i b_n^{\phi}(\lambda)\right] \tag{38}$$

where the coefficient $b_p^*(555)$ for the Potomac River is given by the site-specific equation 34a, and $\eta$ and $\phi_i$ are fixed respectively at 0.502 and 0.0714 (dimensionless), and the function $b_n^{\phi}(\lambda)$ is given in Table 3.

Backscattering is calculated by

$$b_b(\lambda) = B_{532} b_p(\lambda) \tag{39}$$

where $B_{532}$ for the Potomac River is given by the site-specific equation 35; spectral dependence of the backscatter fraction is not considered. The spatial pattern of backscatter fraction shown in Figure 12b may provide some guidance for arriving at the backscatter fraction in other tributaries.

*Model Evaluation*. Predictions of the model are biased slightly negative in comparison with measurements (Figure 14a, black squares). We believe this is due to the presence of vertical gradients, principally in TSS concentrations, wherein model predictions were made using water quality concentrations from a 0.5 m sample. Use of concentrations from a near-bottom sample (depth varied among profiles) consistently overestimated measured $K_d$(PAR) (Figure 14a, open triangles). An example of how vertical variations in water quality can affect model $K_d$(PAR) calculations is given for station PR07 on 24 March 2004 (Figure 14b). The profile of total (less water) absorption at 440 nm increased from about 2.6 $m^{-1}$ at 0.5 m, the depth of the water sample, to ca. 3.5 $m^{-1}$ at 4 m (Figure 14b, red line; absorption at other wavelengths, as well as scattering, varied similarly). The attenuation coefficient calculated as a variable with depth, $K_d(Z) = -[\ln(PAR_Z) - \ln(PAR_{0.5})]/(Z - 0.5)$, increased with depth, resembling the variation in absorption (Figure 14b, black squares and line). Consequently, the diffuse attenuation coefficient calculated by the model (Figure 14b, red triangle) was about 0.3 $m^{-1}$ less than that calculated by log-linear regression of measured PAR with depth (Figure 14b, black triangle). Scaling the TSS concentration by the ratio (1.18) of the integral average of absorption over the depth profile to the value at 0.5 m, i.e. $\int_0^4 a_{t-w}(440, Z)dz \Big/ a_{t-w}(440, 0.5)$, reduced the difference between model-estimated and measured $K_d$(PAR) to 0.14 $m^{-1}$ (<6%), well within the range of replicate $K_d$(PAR) measurements (Figure 14b, red arrow and circle).

Comparison of model predictions with measurements of $K_d$(PAR) calculated from replicate PAR profiles in the Potomac River (done by the Chesapeake Bay Water Quality

Monitoring Program in 2002) provides some context for model evaluation (Figure 14a, red circles). The coefficient of determination for model predictions using 0.5 m sample with measurements (Figure 14a, black squares) was 0.83, compared with 0.93 for replicate $K_d$(PAR) measurements (Figure 14a, red circles). The additional 10% uncertainty in model predictions is easily accounted for by inherent variability of the specific-absorption and –scattering coefficients (Figures 7,9,11).

Model performance using independent measurements made by the Chesapeake Bay Water Quality Monitoring Program (CBP) was understandably worse than it was with the development data (Figure 14c). The scatter was greater ($r^2$=0.57), due in part to using seasonal mean CDOM concentrations rather than measurements. The tendency of the model to underestimate at large $K_d$(PAR) (>2 $m^{-1}$) in the CBP data is, as with the development data, probably due to the presence of vertical gradients in TSS that are not well represented by the 0.5-m sample.

*Sensitivity Analysis.* We examined the sensitivity of model predictions to uncertainty in parameters and water quality concentrations using a bootstrap procedure (Table 4). We assigned probability distributions to model parameters and water quality concentrations based on observed uncertainties in fitted functions (i.e. Figures 5c, 7c, 8c, 9c, 11c,12c) or assumed values (for water quality concentrations). We then determined the uncertainty in calculated $K_d$(PAR) introduced by the given uncertainty in parameter or water quality concentration, both singly and in combination, using the Excel add-in, Crystal Ball™, which assigns random variables from a specified distribution to spreadsheet constants, and calculates the distribution of variables that depend on them, using Monte Carlo simulation (5000 realizations).

We first examined the uncertainty introduced by assuming constant spectral shapes for particulate scattering and absorption by phytoplankton chlorophyll, i.e. by using constant values for $\eta$, $\phi_i$, and $\phi(\lambda)$. For the baseline case we used input data from a sample for which the model performed satisfactorily, 24 March 2004 PR01, predicting $K_d$(PAR)=1.521 $m^{-1}$ compared with an observed value of 1.541 $m^{-1}$. Water quality concentrations for this profile were $a_g(440)$=0.414 $m^{-1}$, CHLA=1.86 mg $m^{-3}$, and TSS=17.08 g $m^{-3}$. Uncertainty in spectral shape of phytoplankton absorption was represented by calculating principal components (PC) on the observed $\phi(\lambda)$, and assigning a standard normal variate to the scores. Three principal components accounted for over 95% of the variance in observed $\phi(\lambda)$. These three sources of uncertainty (i.e. $\eta$, $\phi_i$, and $\phi(\lambda)$ PC scores) resulted in less than 0.5% uncertainty in simulated $K_d$(PAR) singly (Table 4, Section A), and <1% in combination (not shown). We therefore conclude that there is no appreciable uncertainty in calculated $K_d$(PAR) introduced by assumption of constant spectral shapes for scattering and absorption by phytoplankton.

Uncertainty in the other two spectral shape parameters, $s_g$ and $s_p$, had a relatively larger effect on variability in simulated $K_d$(PAR), giving rise to a coefficient of variation of 0.55 and 3.14%, respectively (Table 4, Section A). The combined effect of uncertainty in all shape parameters varied simultaneously was 3.34%. The spectral slopes were more influential because smaller values for the coefficients (i.e. negative errors) extend absorption by the respective component further into the green wavelengths, i.e. the absorption minimum, thereby affecting

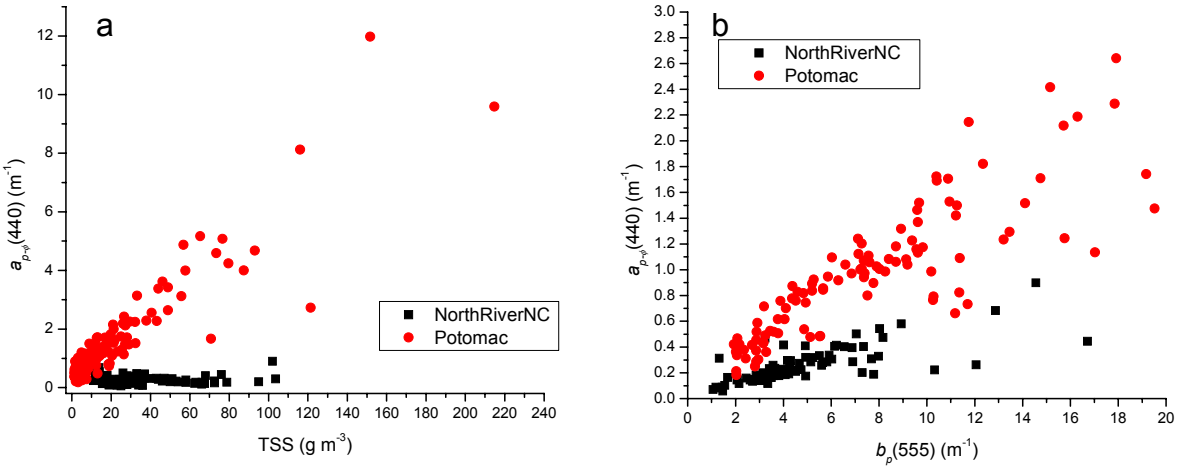


Figure 13. Comparison of NAP absorption for the Potomac River with that of the North River, North Carolina. a) Non-algal particulate absorption at 440 nm versus total suspended solids (TSS). b) Non-algal particulate absorption at 440 nm versus scattering coefficient at 555 nm. Slopes of the relationships indicate that particle color index (PCI), i.e. the ratio of non-algal particulate absorption at 440 nm to particulate scattering at 555 nm, is less variable than specific-absorption coefficients. Data in (b) were truncated to facilitate comparison.

calculated $K_d$(PAR). The converse is true for positive errors. More specifically for this example, $s_p$ was more influential than the other shape parameters because of the dominance of total absorption by NAP for the given water quality concentrations (particularly TSS=17.8 g $m^{-3}$).

For examining effects of uncertainty in scaling parameters and water quality concentrations, we used as a base simulation conditions in which CDOM, chlorophyll, and TSS all had some influence on calculated $K_d$(PAR), and which predicted a $K_d$(PAR) close to the Tier II SAV habitat requirement of 1.5 $m^{-1}$ (Batiuk et al. 2000). Concentrations used were $a_g(440)$=0.5 $m^{-1}$, CHLA=12 mg $m^{-3}$, and TSS=10 g $m^{-3}$, and depth was taken to be 2 m. These inputs gave a calculated $K_d$(PAR)=1.503 $m^{-1}$.

The scaling parameters had a relatively larger effect on variability in simulated $K_d$(PAR), both singly and in combination (Table 4, Section B). This was due both to their larger overall percentage variability (25-50%) and their effect in scaling the magnitude of absorption and scattering. Uncertainty in $a_{p\text{-}\phi}^*(440)$, $a_\phi^*(675)$, and $b_p^*(555)$ resulted in coefficient of variation for $K_d$(PAR) of about 7-10%, while that due to $B_{532}$ was about 5% (Table 4, Section B). The coefficient of variation due to simultaneous variation in all scaling parameters was 16.3% (Table 4, Section B).

To examine the effect of uncertainty in water quality measurements, we first considered equal percentage (10%) uncertainty in each input concentration (Table 4, Section C). For the case considered, 10% variation each input concentration produced <4% coefficient of variation

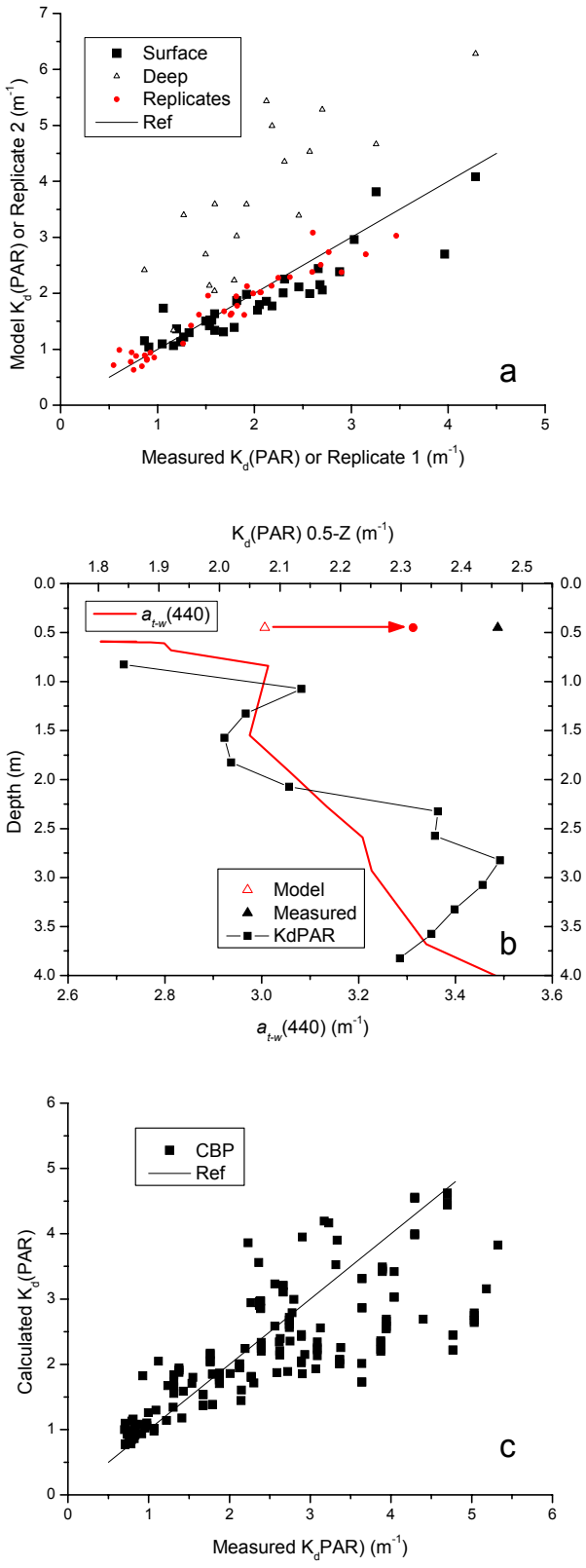


Figure 14. Model evaluation. a) Modeled versus measured diffuse attenuation coefficient, $K_d$(PAR), for surface (black squares) and near-bottom (open triangles) samples. Measurements of $K_d$(PAR) calculated from replicate PAR profiles in the Potomac River, done by the Chesapeake Bay Water Quality Monitoring Program in 2002, are shown as red circles. b) Vertical profiles of absorption at 440 nm (total-water, red line) and $K_d$(PAR) (black squares and line) profiles for station PR07 on 24 March, 2004. The red triangle shows $K_d$(PAR) calculated by the mode using water quality concentrations from the 0.5-m sample, while the black triangle shows $K_d$(PAR) calculated by log-linear regression of measured PAR with depth. The red circle and arrow show the estimated $K_d$(PAR) when the total suspended solids concentration is scaled by the ratio of the integral average of absorption over the depth profile to the value at 0.5 m. c) Modeled versus measured $K_d$(PAR) using independent measurements made by the Chesapeake Bay Water Quality Monitoring Program (CBP). The 1:1 line is drawn for reference.

in simulated $K_d$(PAR). The rank order was TSS>CHLA>$a_g$(440). To examine the effect of simultaneous variation in all input concentrations, we assumed more realistic percentage uncertainty in input concentrations: CDOM (5%); CHLA (15%); TSS (30%). The resulting coefficient of variation in simulated $K_d$(PAR) was 10.84% (Table 4, Section C).

To examine the effect of simultaneous uncertainty in parameters, it is necessary to consider two situations, one in which errors are correlated, and one in which they are not. When evaluating the model against data for which optical measurements are available, as in the development data, a positive error in measurement of TSS will result in a corresponding negative error in coefficients that depend on TSS in the denominator, i.e. $a_{p\text{-}\phi}^*$(440) and $b_p^*$(555). The converse is true for negative errors in TSS. For this case, we assumed a correlation coefficient between errors in TSS and the coefficients $a_{p\text{-}\phi}^*$(440) and $b_p^*$(555) of -0.67. The resulting coefficient of variation in simulated $K_d$(PAR) was 15% (Table 4, Section D). When evaluating the model against independent data for which no estimates of the specific-absorption and -scattering coefficients are available (i.e. CBP data), there is no reason to expect negatively correlated errors. Removing the correlations increases the simulated coefficient of variation to about 20% (Table 4, Section D).

The conclusions of the sensitivity analysis are necessarily specific to the conditions assumed for the base condition. For example, the same analysis for conditions in a black-water system such as the Pocomoke River would show larger influence of CDOM related parameters. Similarly, simulation of uncertainty under phytoplankton bloom conditions would show larger effects of errors in CHLA and $a_\phi^*$(675). The conditions assumed are relevant to the use of the model for determining the efficacy of management efforts to restore conditions conducive to growth of SAV. Neither the available data nor the approach taken enable us to quantitatively assess the effect of vertical gradients in water quality on prediction uncertainty. Vertical gradients do, however, lead to underestimates by the model, which apparently add to the overall scatter in comparisons of predicted and observed (Figure 14c). While such gradients are unavoidable in field data, in coupled circulation-water quality simulations, the vertical gradient in concentrations will be known, and integral averages can be used, thereby minimizing the effects of gradients. In that case, a standard deviation of 0.31 $m^{-1}$ in $K_d$(PAR) would appear to be a reasonable estimate of the uncertainty, with the possibility of further reduction to ca. 0.25 $m^{-1}$ if further optical measurements become available.

Table 4. Uncertainty (standard deviation, $m^{-1}$, and coefficient of variation) in calculated $K_d$(PAR) due to variation in parameters and water quality concentrations. Base value or source for the parameter is given in parentheses. Uncertainty in parameters was simulated either as additive [normally distributed errors, N(mean, standard deviation)] or multiplicative [lognormally distributed errors, LN(mean, standard deviation)].

| Parameter | Error Distribution | Mean $K_d$(PAR) ($m^{-1}$) | Standard Deviation ($m^{-1}$) | Coefficient of Variation |
|---|---|---|---|---|
| **Section A** | **Spectral Shape Parameters** | | | |
| $\eta$ (0.502) | N(0, 0.2) | 1.521 | 0.0075 | 0.49% |
| $\phi_i$ (0.7) | N(0,0.02) | 1.521 | 0.0023 | 0.15% |
| $\phi(\lambda)$ PC scores (0) | N(0,1) | 1.521 | 0.0073 | 0.48% |
| $s_g$ (Eq. 31) | N(0,0.002) | 1.522 | 0.00832 | 0.55% |
| $s_p$ (Eq. 32) | N(0,0.00064) | 1.523 | 0.0478 | 3.14% |
| All combined | As above | 1.525 | 0.0510 | 3.34% |
| **Section B** | **Scaling Parameters** | | | |
| $a_{p\text{-}\phi}^*(440)$ (Eq. 33a) | LN(1,0.39) | 1.508 | 0.1446 | 9.59% |
| $a_\phi^*(675)$ (0.0223)<br>$\phi(\lambda)$ PC scores | N(0.0104,0.02)<br>N(0,1) | 1.574 | 0.1588 | 10.1% |
| $b_p^*(555)$ (Eq. 34a) | LN(1.0,0.24) | 1.505 | 0.1092 | 7.26% |
| $B_{532}$ (Eq.35) | N(0,0.000451) | 1.497 | 0.0824 | 5.50% |
| All combined | As above | 1.574 | 0.2570 | 16.3% |
| **Section C** | **Water Quality Concentrations** | | | |
| $a_g(440)$ | LN(1.0,0.1) | 1.503 | 0.0085 | 0.57% |
| CHLA | LN(1.0,0.1) | 1.503 | 0.0274 | 1.82% |
| TSS | LN(1.0,0.1) | 1.500 | 0.0509 | 3.38% |
| WQ combined | LN(1,0.05), LN(1,0.15), LN(1,0.3) | 1.508 | 0.1630 | 10.84% |
| **Section D** | **Parameters and Water Quality Combined** | | | |
| | As above, errors correlated (see text) | 1.539 | 0.2310 | 15.0% |
| | As above, errors uncorrelated | 1.578 | 0.3096 | 19.62% |

## Model Simplification

The 22 equations of Table 2, while simple to solve and easily implemented in a spreadsheet, have the potential to place a considerable time burden on a three-dimensional water quality simulation with many thousands of grid cells. We therefore sought a simplified implementation that maintains the flexibility to vary the parameters shown to be important by the sensitivity analysis. We chose a lookup table approach by discretizing the major factors controlling the magnitude of $K_d$(PAR).

In view of the foregoing sensitivity analysis, it is clear that variations in the spectral shape parameters are of less importance than the scaling parameters and water quality concentrations. Moreover, it is the product of the scaling coefficient and water quality concentration that determines the effect of a constituent on total absorption and scattering (i.e. equations 5a, 5b, 6d). We therefore generated an array of simulated $K_d$(PAR) in nested loops of varying CDOM absorption $a_g(440)$, phytoplankton absorption $a_\phi^*(675)$[CHLA], particulate scattering $b_p^*(555)$[TSS], NAP absorption $b_p^*(555)$[TSS]*PCI*, along with solar zenith angle $\mu_0$, and backscatter fraction $B_{532}$. To do this, bin boundaries for the preceding quantities were generated which are thought to cover the likely range of conditions reasonably encountered (Table 5). We then calculated $K_d$(PAR) by full solution of equations at the midpoints of the bins, and recorded index variables for each of the loop variables. Bin boundaries are given in Table 5. Bin widths for the primary absorption and scattering magnitudes increased exponentially, in keeping with the tendency for proportional scatter with increasing $K_d$(PAR) (Figures 14c). The calculations with nested loops resulted in 1,920,000 discrete values of $K_d$(PAR). Simulated $K_d$(PAR) ranged from <0.3 to >50 $m^{-1}$ (distribution of values shown in Figure 15a), and so should more than cover the range of values encountered in Chesapeake Bay.

The simplified model operates by determining index variables for the governing parameters by comparing values for the current time step and location with bin boundaries, and pulling the appropriate value of $K_d$(PAR) from the table. The algorithm allows for regionally (by Chesapeake Bay segment) and seasonally (4) variable CDOM concentrations, specific-absorption and –scattering coefficients, and backscattering coefficient, and temporally (by day of year) solar zenith angle. As an example, any combination of chlorophyll concentration and chlorophyll-specific absorption meeting the criteria $0.2723 < a_\phi^*(675)[CHLA] \le 0.3915$ will map to the 10th chlorophyll bin (Table 5). Given the potential range of $a_\phi^*(675)$ (Magnuson et al. 2004), a rather wide range of chlorophyll concentrations can potentially fall within this bin (Figure 15b, green region).

Values for the specific-absorption and –scattering coefficients on a Chesapeake Bay segment basis are read in from files. Presently there are relatively few direct measurements of these parameters around the Bay, so many values are defaulted at reasonable values which may or may not be accurate. These files will be updated as measurements become available. Presently, there is considerable scatter ($r^2$=0.55, mean measured-calculated = -0.137 $m^{-1}$ significantly <0, P<0.0001) in the predictions (Figure 16a), due to uncertainty (and inherent variability) in these parameters. We are, however, experimenting with a process for estimating the parameters using an inverse procedure. The procedure involves using the Excel add-in, *Solver*, to adjust the parameters $b_p^*(555)$ and *PCI* to minimize the squared residual between

model and measured median $K_d$(PAR) with the median CHLA and TSS concentrations as input. An example is presented in Figure 16b for the oligohaline Mataponi River (segment MPNOH), which showed a large, systematic underestimation (mean observed-calculated = 1.9 $m^{-1}$) with the parameter values initially used (Figure 16b, black squares). Application of the inverse routine resulted in revision of $b_p^*(555)$ from 0.36 to 1.0 $m^2$ $g^{-1}$, and *PCI* from 0.2 to 0.126, and substantially improved estimates (Figure 16b, red circles). We believe application of this procedure, after testing in systems with measured parameters for comparison, may substantially improve the performance of the lookup table approach with measured data.

In summary, the simplified model based on a lookup table approach is fast and flexible, and capable of incorporating information on spatial and seasonal variability in inherent optical properties as it becomes available. Documenting that spatial and temporal variability of inherent optical properties is a high priority for correctly predicting the effects of management actions on improvement of water clarity in Chesapeake Bay.

Table 5. Bin boundaries for absorption by CDOM, chlorophyll, non-algal particles, scattering, backscattering, and solar zenith angle.

| Index | $a_g(440)$ | $a_\phi(657)$ | $b_p(555)$ | $B_{532}$ | *PCI* | $\mu_0$ |
|---|---|---|---|---|---|---|
| 1 | 0.0565 | 0.0051 | 0.7191 | 0.0060 | 0.075 | 0.78 |
| 2 | 0.1794 | 0.0124 | 1.6423 | 0.0100 | 0.110 | 0.82 |
| 3 | 0.3165 | 0.0226 | 2.8279 | 0.0140 | 0.145 | 0.86 |
| 4 | 0.4696 | 0.0372 | 4.3501 | 0.0180 | 0.180 | 0.90 |
| 5 | 0.6405 | 0.0580 | 6.3047 | 0.0220 | 0.215 | 0.94 |
| 6 | 0.8313 | 0.0874 | 8.8144 | 0.0260 | 0.250 | |
| 7 | 1.0442 | 0.1291 | 12.0370 | 0.0300 | | |
| 8 | 1.2819 | 0.1883 | 16.1749 | 0.0340 | | |
| 9 | 1.5472 | 0.2723 | 21.4880 | | | |
| 10 | 1.8434 | 0.3915 | 28.3102 | | | |
| 11 | 2.1740 | 0.5607 | 37.0701 | | | |
| 12 | 2.5431 | 0.8007 | 48.3180 | | | |
| 13 | 2.9551 | 1.1414 | 62.7606 | | | |
| 14 | 3.4150 | 1.6249 | 81.3052 | | | |
| 15 | 3.9283 | 2.3109 | 105.1170 | | | |
| 16 | 4.5014 | 3.2844 | 135.6920 | | | |
| 17 | 5.1411 | 4.6660 | 174.9510 | | | |
| 18 | 5.8551 | 6.6264 | 225.3606 | | | |
| 19 | 6.6523 | 9.4084 | 290.0878 | | | |
| 20 | 7.5420 | 13.3563 | 373.1992 | | | |

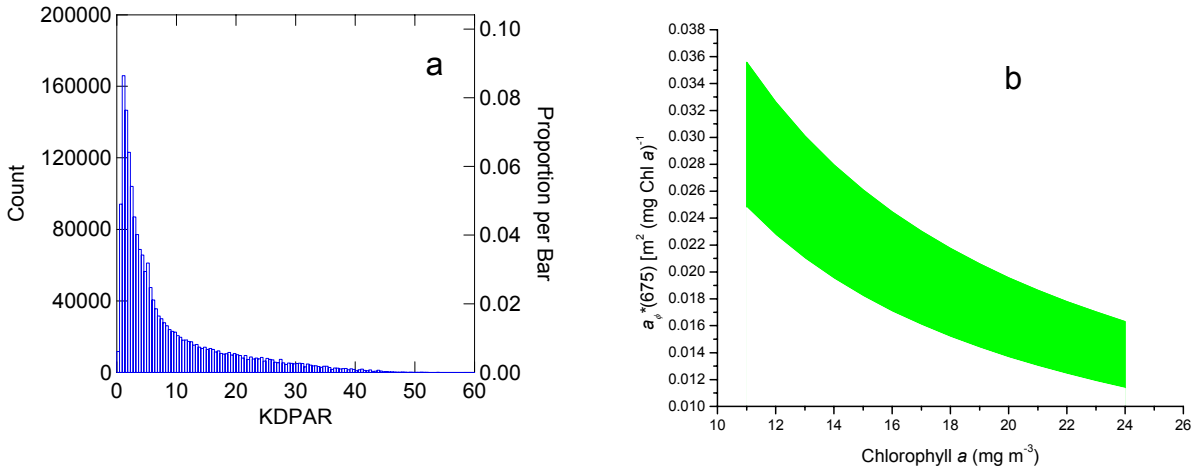


Figure 15. a) Frequency histogram of discrete values (1,920,000) of $K_d$(PAR) comprising the lookup table for the simplified model. b) Green shaded region delimits combinations of chlorophyll concentration and chlorophyll-specific absorption coefficient that produce values of $a_\phi$(675) within the 10th bin for chlorophyll absorption, i.e. (see Table 5).

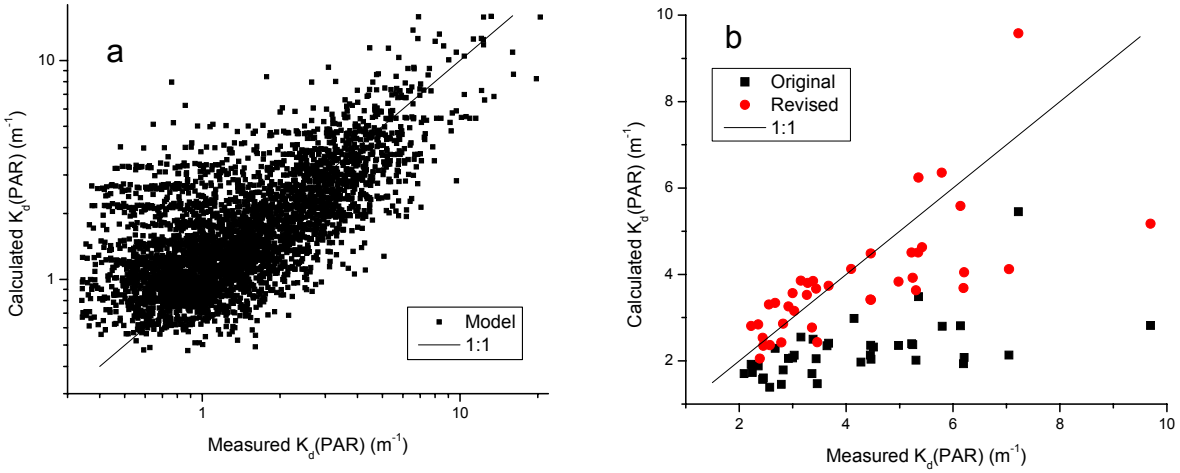


Figure 16. a) Diffuse attenuation coefficients for PAR calculated by the lookup table approach plotted against measured values from the Chesapeake Bay Water Quality Monitoring Program, 1995-1999; 1:1 line is provided for reference. b) Diffuse attenuation coefficients for PAR calculated by the lookup table approach plotted against measured values for oligohaline Mataponi River (MPNOH) with (black squares) originally estimated values for specific-scattering coefficient and particle color index, and (red circles) adjusted parameters determined using an inverse solution on median measured $K_d$(PAR) and water quality concentrations.

**Acknowledgements**

Funds for this investigation were provided through the US Army Engineer Baltimore District. Project administrator was Ms. Jean Kapusnick. Technical administration was provided by Carl F. Cerco, who also provided helpful comments on a previous draft. We would like to thank Steve Suttles, Grace Cartwright, Patrick Dickhudt, Shih-Nan Chen and Sam Benson for assistance in the field. Additionally we thank Darrick Sparks for assistance in both the field and laboratory.

**References**

Albert, A., Mobley, C.D., 2003. An analytical model for subsurface irradiance and remote sensing reflectance in deep and shallow case-2 waters. Optics Express 11, 2873-2890.

Babin, M., Stramski, D., 2004. Variations in the mass-specific absorption coefficient of mineral particles suspended in water. Limnology and Oceanography 49, 756-767.

Batiuk, R.A., Bergstrom, P., Kemp, W.M., Koch, E.W., Murray, L., Stevenson, J.C., Bartleson, R., Carter, V., Rybicki, N.B., Landwehr, J.M., Gallegos, C.L., Karrh, L., Naylor, M., Wilcox, D.J., Moore, K.A., Ailstock, S., Teichberg, M., 2000. Chesapeake Bay submerged aquatic vegetation water quality and habitat-based requirements and restoration targets: A second technical synthesis. U. S. Environmental Protection Agency, Annapolis, Maryland.

Boss, E., Twardowski, M.S., Herring, S., 2001. Shape of the particulate beam attenuation spectrum and its inversion to obtain the shape of the particulate size distribution. Applied Optics 41, 4885-4893.

Bowers, D.G., Binding, C.E., 2006. The optical properties of mineral suspended particles: A review and synthesis. Estuarine, Coastal and Shelf Science 67, 219-230.

Bricaud, A., Bédhomme, A.-L., Morel, A., 1988. Optical properties of diverse phytoplantonic species: experimental results and theoretical interpretation. Journal of Plankton Research 10, 851-873.

Cuthbert, I.D., del Giorgio, P., 1992. Toward a standard method of measuring color in freshwater. Limnology and Oceanography 37, 1319-1326.

Gallegos, C.L., 2005. Optical water quality of a blackwater river estuary: the Lower St. Johns River, Florida, USA. Estuarine, Coastal and Shelf Science 63, 57-72.

Kirk, J.T.O., 1984. Dependence of relationship between apparent and inherent optical properties of water on solar altitude. Limnology and Oceanography 29, 350-356.

Kirk, J.T.O., 1981. Monte Carlo study of the nature of the underwater light field in, and the relationships between optical properties of, turbid, yellow waters. Australian Journal of Marine and Freshwater Research 32, 517-532.

Kirk, J.T.O., 1994. The relationship between the inherent and the apparent optical properties of surface waters and its dependence on the shape of the volume scattering function. In: Spinrad, R.W., Carder, K.L. and Perry, M.J. (Eds.), Ocean optics. Oxford University Press, New York, pp. 40-58.

Kishino, M., Takahashi, M., Okami, N., Ichimura, S., 1985. Estimation of the spectral absorption coefficients of phytoplankton in the sea. Bulletin of Marine Science 37, 634-642.

Magnuson, A., Harding, L.W. Jr., Mallonee, M.E., Adolf, J.E., 2004. Bio-optical model for Chesapeake Bay and the Middle Atlantic Bight. Estuarine, Coastal and Shelf Science 61, 403-424.

Mobley, C.D., 1994. Light and water. Radiative transfer in natural waters. Academic Press, New York.

Pope, R.M., Fry, E.S., 1997. Absorption spectrum (380-700) nm of pure water. II. Integrating cavity measurements. Applied Optics 36, 8710-8723.

Vodacek, A., Blough, N.V., DeGrandpre, M.D., Peltzer, E.T., Nelson, R.K., 1997. Seasonal variation of CDOM and DOC in the Middle Atlantic Bight: Terrestrial inputs and photooxidation. Limnology and Oceanography 42, 674-686.